

# 3-D Imaging Based on Combination of the ISAR Technique and a MIMO Radar System

Yong Wang<sup>1</sup>, Senior Member, IEEE, and Xuelu Li

**Abstract**—In this paper, a novel 3-D imaging method achieved by combining the inverse synthetic aperture radar (ISAR) technique and a multiple-input-multiple-output (MIMO) radar system is presented. The high-resolution image of a target can be obtained within a limited imaging time interval, and the computational load can be reduced simultaneously because the time samples obtained by the ISAR technique can be used to play the role of space samples needed in the MIMO radar system. The adopted process of time selection method can help to realize the exact combination of the signals received by different antenna elements without producing nonequivalence between the time samples and the space samples which need to be substituted. Besides, the 2-D smoothed (2-D SLO) method, which is especially designed for 2-D signals in the compressed sensing (CS) technique, is used to realize the high-resolution imaging when there are gaps in the global observation angle without increasing the computation load or introducing the false estimated data. Furthermore, the algorithms for range alignment and velocity estimation under the 3-D imaging radar configuration are described explicitly. Finally, the simulation results are provided to prove the effectiveness of the algorithms proposed in this paper.

**Index Terms**—3-D reconstruction, compressed sensing (CS) technique, inverse synthetic aperture radar (ISAR), multiple-input-multiple-output (MIMO) radar system, range alignment, velocity estimation.

## I. INTRODUCTION

INVERSE synthetic aperture radar (ISAR) can be used to produce high-resolution 2-D images from long range. The ISAR imaging technique has received much attention in the past decades for its high value in military and civil applications [1]–[10]. The traditional 2-D ISAR image is obtained by projecting the real spatial 3-D target onto the range-Doppler plane, and thus it cannot provide real information about the scatterer positions without the knowledge about the imaging resolution. The result is that the 2-D ISAR images can only deliver limited information to the subsequent automatic target recognition and classification work. Several efficient 3-D ISAR imaging algorithms based on 2-D imaging techniques have been proposed to remedy the disadvantages of traditional ISAR

images [11]–[25]. Among these methods, the 3-D interferometric ISAR (InISAR) imaging technique associated with the multiple-input-multiple-output (MIMO) radar system has received much attention for their robustness and convenient implementation. However, the 3-D InISAR imaging techniques have some disadvantages, which cannot be easily avoided. First, the 3-D InISAR imaging is implemented based on the 2-D ISAR images, which means that the accurate and complex motion compensation for the noncooperate targets is necessary during the imaging process. Furthermore, the imaging quality of the 3-D InISAR technique is directly related to the image quality of the 2-D ISAR images. If the scatterers in the 2-D ISAR images are not separated successfully or the phase information is not preserved correctly, the 3-D coordinates of the targets cannot be reconstructed as accurately as one desired. For targets with nonuniform motions such as the airplanes with complex maneuvers and ship targets in rough sea condition, it is very hard to get the ideal ISAR images to realize 3-D InISAR imaging. Special imaging algorithms must be designed to achieve some relatively satisfactory ISAR images, and many existing algorithms cannot be utilized since they cannot meet the demand that the phase information must be preserved as required in the 3-D InISAR imaging technique.

Alternatively, the 3-D imaging technique based on the MIMO radar system can avoid all the disadvantages in the 3-D InISAR imaging as mentioned above. The MIMO radar system can transmit multiple independent orthogonal signals from multiple antennas (transmitters) and receive the return signals using multiple receiving antennas (receivers), according to the phase center approximation (PCA) theory in [26], which can enable it to form plenty of equivalent virtual independent antenna elements (transceivers) that can transmit and receive signals at the same time in the space domain. As in a phased-array radar system, the MIMO radar system can use space samples from different transceivers at one snapshot (one pulse) to replace time samples from one transceiver over a long time, which has been utilized in the synthetic aperture radar system, to form 2-D images. At the same time, although sharing a similar imaging principles, the MIMO radar system can obtain the images with less transmitters and receivers by transmitting orthogonal signals, excepted for the other advantages over the conventional phased array, as described in [27]–[29]. In this way, the complex motion compensation process which is required for the synthetic aperture radar system can be avoided. Besides, even for targets with nonuniform motions, such as airplanes and ships as mentioned above, producing

Manuscript received February 6, 2018; accepted April 20, 2018. Date of publication May 21, 2018; date of current version September 25, 2018. This work was supported by the National Natural Science Foundation of China under Grant 61471149 and Grant 61622107. (Corresponding author: Yong Wang.)

The authors are with the Research Institute of Electronic Engineering Technology, Harbin Institute of Technology, Harbin 150001, China (e-mail: wangyong6012@hit.edu.cn).

Color versions of one or more of the figures in this paper are available online at <http://ieeexplore.ieee.org>.

Digital Object Identifier 10.1109/TGRS.2018.2829912

0196-2892 © 2018 IEEE. Personal use is permitted, but republication/redistribution requires IEEE permission. See [http://www.ieee.org/publications\\_standards/publications/rights/index.html](http://www.ieee.org/publications_standards/publications/rights/index.html) for more information.

ideal 2-D images for them is no longer a problem since the 2-D images are obtained in an extremely short time, namely, one snapshot, so that the complex motion of the targets will not play a role in changing the image projection planes of the images. Combined with the range information obtained by transmitting wideband signals in the MIMO radar system, the information obtained in two different directions from the 2-D images can help to reconstruct the coordinates of the targets easily.

Nevertheless, the much higher computational load of the MIMO radar system cannot be negligible compared with those of the traditional synthetic aperture radar system. As a result, the idea that combining the time samples with space samples, that is, adopting the ISAR technique in the MIMO radar imaging process, to improve the imaging resolutions is proposed [22], [30], [31]. In this way, the computational load can be much reduced and the imaging time will be short for the ISAR technique adopted in the MIMO radar system. What is more, the nonuniform motions of the target during the aperture synthesis time (imaging time) will not degrade the imaging results. In [30], a complete imaging process flow showing how to combine the signals obtained in the distributed radar system with linear arrays is proposed. The cases of the time samples are insufficient to compensate the space interval or the antenna array are nonlinear are not considered. In [31], the complete imaging algorithms for the situation whether or not the time samples can compensate the whole space interval are analyzed efficiently. The procedure for time selection should be studied and the interpolation method in [32] can consequently be avoided. In [22], the multiple images obtained through the MIMO radar system with multiple snapshots are combined efficiently, and thus the imaging results become clearer with high signal-to-noise ratio (SNR), although the imaging resolution is not obviously improved.

In this paper, we propose an effective algorithm to better combine the ISAR technique with the MIMO radar system for the purpose of improving the imaging resolution. The main contribution of this paper can be concluded as follows.

- 1) The compressed sensing (CS) technique is used for data compensation.

Different from the methods in [31] and [32], the CS technique is used to replace the interpolation process to solve the problem occurring when the time samples are insufficient to compensate the whole space interval; thus, there are gaps in the global observation angle for the radar system. Due to the reason that the number of scatterers is always smaller than the number of pixels in the images obtained by the radar systems, either through the ISAR technique or the MIMO radar system, the image can be regarded as a sparse representation of the echoes. As a result, we can use the CS technique to realize the imaging process and obtain the image with high quality even in the situation where the numbers of the transmitters and receivers are limited or the obtained data are not complete. The CS technique is a novel sampling theory and has been used for processing radar signals in many situations [33]–[37].

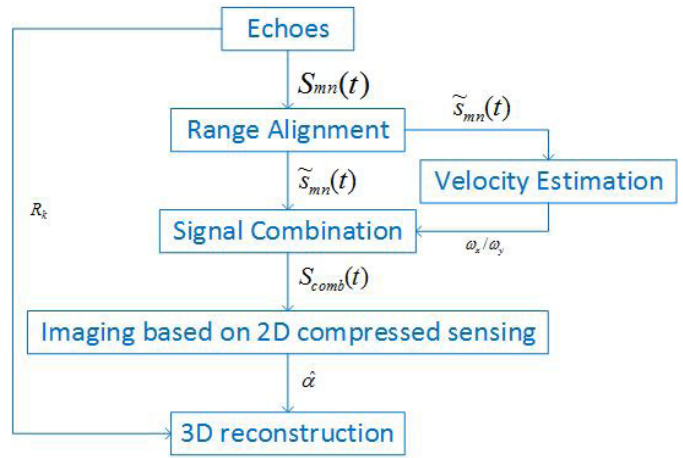


Fig. 1. Imaging flowchart.

- 2) The extension of the 2-D smoothed  $l_0$  method for imaging under planar arrays.

In this paper, we extend the algorithm to planar arrays to realize the 3-D high-resolution imaging based on the MIMO radar system, and the CS method which is specifically designed for the 2-D signals, namely, the 2-D SL0 method, is adopted to solve the specific imaging problem discussed in this paper.

- 3) The specific procedure design for the range alignment and the velocity estimation processes.

Some special imaging procedures such as range alignment and velocity estimation especially designed for the imaging configuration in this paper will be presented explicitly.

This paper is organized as follows. In Section II, the signal model in the MIMO radar system is introduced. In Section III, the combination of the MIMO radar system and the ISAR technique is presented. In Section IV, the imaging process based on a 2-D CS technique is described. In Section V, the process of range alignment and the process of velocity estimation especially for the designed radar configuration are introduced. The experimental results are shown in Section VI. The conclusion is provided in Section VII.

First, in order to give a brief idea about the whole process of the 3-D imaging method designed in this paper, the imaging flowchart is shown in Fig. 1.

## II. SIGNAL MODEL

The configuration of a MIMO radar system designed in this paper is shown in Fig. 2, where the transmitting planar array consists of  $M_1 \times M_2$  antenna elements, and the receiving planar array consists of  $N_1 \times N_2$  antenna elements. The distances between the adjacent antenna elements in the dimensions of the transmitting array and the receiving array are  $d_t$  and  $d_r$ , respectively. Here, for convenience, we suppose that the distances between the adjacent antennas in the two dimensions are the same for either the transmitting antenna array or the receiving antenna array. Fig. 3 shows the plan view of the MIMO radar system configuration in Fig. 2. According to

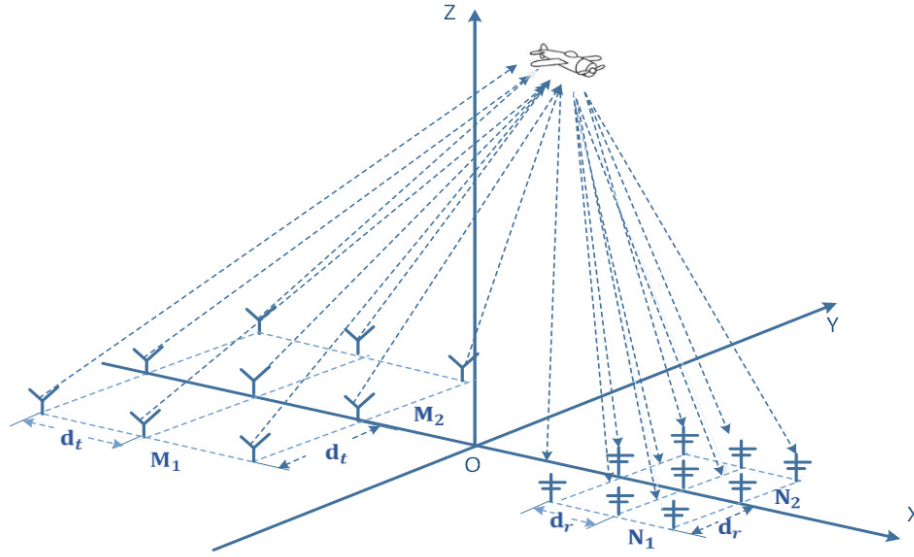


Fig. 2. Configuration of the MIMO radar system.

the PCA theory, it is easy to figure out that a virtual planar array consisting of  $M_1 N_1 \times M_2 N_2$  antenna elements which can transmit and receive signals at the same time can be formed. Besides, it is easy to prove that when conditions  $d_t = N_1 d_r$  and  $N_1 = N_2$  are satisfied, the distances between the adjacent elements of the virtual planar array in two dimensions will become  $d$  (where  $M_1, M_2, N_1, N_2, M_1 N_1$ , and  $M_2 N_2$  represent the numbers of the antenna elements in each row and each column in the corresponding antenna arrays), and  $d = d_r/2$ . It should be noted that when  $N_2 = M_2 = 1$ , the transmitting and the receiving planar arrays will become linear arrays, and the virtual planar array formed will also become linear.

We can choose the phase shift key signals as the transmitting signals due to their convenience in designing the required orthogonal signals in the MIMO radar system. Details about the signal formation can be seen in [38].

According to the working principle of the MIMO radar system in [39], the received signal at the  $n$ th receiver transmitted by the  $m$ th transmitter can be expressed as follows after the matched filtering process:

$$S_{mn}(t) = \sum_k \sum_p \alpha_k r_m \left( t - pT_p - \frac{R_{mpk}^t + R_{npk}^r}{c} \right) \cdot \exp \left( -j \frac{2\pi f_c}{c} (R_{mpk}^t + R_{npk}^r) \right) \quad (1)$$

where  $T_p$  is the pulse repetition interval,  $f_c$  is the carrier frequency, and  $p$  is the pulse index.  $r_m(t)$  denotes the auto-correlation function of the waveform transmitted by the  $m$ th transmitter,  $\alpha_k$  represents the reflection amplitude of the  $k$ th scatterer,  $c$  is the light speed,  $R_{mpk}^t$  is the distance between the  $m$ th transmitter and the  $k$ th scatterer, and  $R_{npk}^r$  is the distance between the  $m$ th scatterer, and the  $n$ th receiver at the  $p$ th pulse.

The received signal after range alignment and phase compensation can be expressed as

$$\tilde{S}_{mn}(t) = \sum_k \sum_p \alpha_k r_m \left( t - \frac{2R_k}{c} \right) \cdot \exp \left( -j \frac{2\pi f_c}{c} (R_{mpk}^t + R_{npk}^r - R_{mpo}^t - R_{npo}^r) \right) \quad (2)$$

where  $R_k$  is the equivalent distance between the  $k$ th scatterer and the center of the equivalent planar array during the first pulse.  $R_{mpo}^t$  and  $R_{npo}^r$  are the distances between the  $m$ th transmitter to the reference point at the  $p$ th pulse and the distance between the reference point to the  $n$ th receiver at the  $p$ th pulse.

We assume that the antenna indices  $m$  and  $n$  can be expressed as

$$m = (m_1, m_2), \quad (m_1 = 0, \dots, M_1 - 1; m_2 = 0, \dots, M_2 - 1)$$

and

$$n = (n_1, n_2), \quad (n_1 = 0, \dots, N_1 - 1; n_2 = 0, \dots, N_2 - 1).$$

Then, the positions of the  $m$ th transmitter and the  $n$ th receiver are  $(m_1 d_t + u_{t0}, m_2 d_t + v_{t0}, 0)$  and  $(n_1 d_r + u_{r0}, n_2 d_r + v_{r0}, 0)$ , respectively, where  $(u_{t0}, v_{t0}, 0)$  and  $(u_{r0}, v_{r0}, 0)$  are the positions of the first transmitter and the first receiver. For the convenience of expression, we assume that  $u_{t0} = v_{t0} = u_{r0} = v_{r0} = 0$ .

As shown in Fig. 4, it is assumed that  $O_0$  on the  $Z$ -axis is the reference point of the target at the initial time. We can construct the coordinate system  $(O_0, \hat{x}, \hat{y}, \hat{z})$ , whose coordinate axes have the same directions as the coordinate system  $(O, X, Y, Z)$ . There is an arbitrary scatterer with the position  $(\hat{x}_0^k, \hat{y}_0^k, \hat{z}_0^k)$  in  $(O_0, \hat{x}, \hat{y}, \hat{z})$ . Supposing the position of the

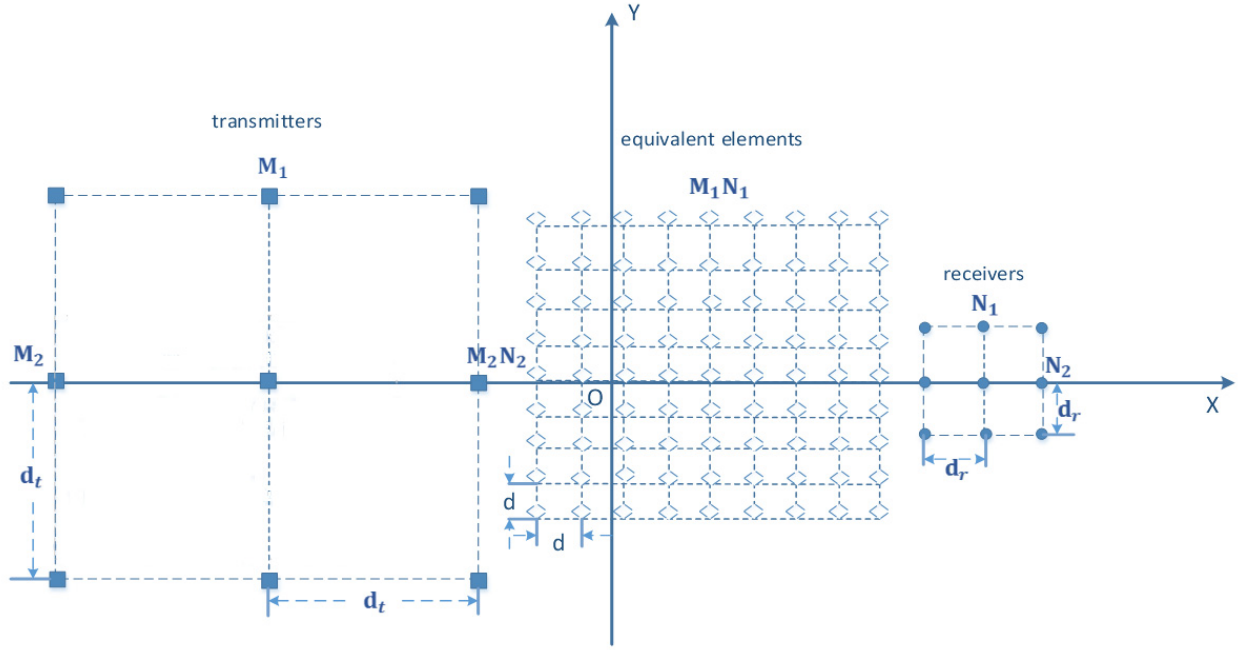


Fig. 3. Planar view of the configuration of the MIMO radar system.

equivalent transceiver at the  $a$ th row and  $b$ th column is

$$\begin{cases} X_a = (a-1)d, a = 1, 2, \dots, M_1 N_1 \\ Y_b = (b-1)d, b = 1, 2, \dots, M_2 N_2 \end{cases} \quad (3)$$

$$\begin{cases} a = m_1 N_1 + n_1 + 1 \\ b = m_2 N_2 + n_2 + 1. \end{cases} \quad (4)$$

Then, the distances from the reference point and the  $k$ th point on the target to  $(X_a, Y_b)$  at the  $p$ th pulse are shown in the following equations, respectively:

$$R_{ab}^p \approx \frac{R_{mpo}^t + R_{npo}^r}{2}, \quad \begin{matrix} a = 1, 2, \dots, M_1 N_1 \\ b = 1, 2, \dots, M_2 N_2 \end{matrix} \quad (5)$$

$$R_{abk}^p \approx \frac{R_{mpk}^t + R_{npk}^r}{2}. \quad (6)$$

In this paper, all the parameters have been selected to satisfy the conditions to avoid the potential imaging failure which may be brought by the approximations of (5) and (6). More details will be found in [26] about how the approximations will affect the final results.

We can rewrite (2) as follows:

$$\begin{aligned} \tilde{S}_{ab}(t) = \sum_k \sum_p \alpha_k r_m \left( t - \frac{2R_k}{c} \right) \\ \times \exp \left( -j \frac{4\pi f_c}{c} (R_{abk}^p - R_{ab}^p) \right). \end{aligned} \quad (7)$$

It is assumed that at the  $p$ th pulse, the reference point  $O_0$  has moved to the position of  $O_p$ , and the coordinate system  $(O_0, \hat{x}, \hat{y}, \hat{z})$  has become  $(O_p, \hat{x}_p, \hat{y}_p, \hat{z}_p)$  after the rotation.  $\theta_p$ ,  $\phi_p$ , and  $\gamma_p$  are the rotation angles in the three dimensions corresponding to the rotation axes  $X$ ,  $Y$ , and  $Z$ . Now, the position of the arbitrary point in the reference coordinate system has changed from  $(\hat{x}_0^k, \hat{y}_0^k, \hat{z}_0^k)$  to  $(\hat{x}_p^k, \hat{y}_p^k, \hat{z}_p^k)$ .

Since

$$\begin{aligned} R_{abk}^p - R_{ab}^p &= \sqrt{(R_{ab}^p + \hat{z}_{abp}^k)^2 + (\hat{y}_{abp}^k)^2 + (\hat{x}_{abp}^k)^2} - R_{ab}^p \\ &= \sqrt{(R_{ab}^p)^2 + 2R_{ab}^p \hat{z}_{abp}^k + (\hat{r}_{abp}^k)^2} - R_{ab}^p \\ &\approx \hat{z}_{abp}^k + \frac{(\hat{r}_{abp}^k)^2}{2R_{ab}^p} \end{aligned} \quad (8)$$

where  $(\hat{x}_{abp}^k, \hat{y}_{abp}^k, \hat{z}_{abp}^k)$  are the coordinates of the  $k$ th scatterer at the  $p$ th pulse relative to the equivalent transceiver at the position  $(X_a, Y_b)$  and  $(\hat{r}_{abp}^k)^2 = (\hat{x}_{abp}^k)^2 + (\hat{y}_{abp}^k)^2 + (\hat{z}_{abp}^k)^2$ . According to the 3-D rotation geometrical relationship (it should be noted that  $\phi_p$  has a different rotation direction compared with the other two as shown in Fig. 4) and  $\hat{r}_{abp}^k \ll R_{ab}^p$ , we can obtain

$$\begin{aligned} R_{abk}^p - R_{ab}^p &\approx \hat{z}_{abp}^k = \hat{x}_0^k \sin(\phi_{ab}^0 + \phi_p) + \hat{y}_0^k \sin(-\alpha_{ab}^0 + \theta_p) \\ &\quad \cdot \cos(\phi_{ab}^0 + \phi_p) + \hat{z}_0^k \cos(-\alpha_{ab}^0 + \theta_p) \cos(\phi_{ab}^0 + \phi_p) \end{aligned} \quad (9)$$

where  $\alpha_{ab}^0$  and  $\phi_{ab}^0$  are the azimuth angle and the grazing angle of the equivalent antenna element at  $(X_a, Y_b)$  relative to the point  $O$ .

As a result, we can rewrite (7) as

$$\begin{aligned} \tilde{S}_{ab}(t) = \sum_k \sum_p \alpha_k r_m \left( t - \frac{2R_k}{c} \right) \\ \times \exp \left( -j \frac{4\pi f_c}{c} \left( \hat{x}_0^k \sin(\phi_{ab}^0 + \omega_x p T_p) \right. \right. \\ \left. \left. + \hat{y}_0^k \sin(-\alpha_{ab}^0 + \omega_y p T_p) \cos(\phi_{ab}^0 + \omega_x p T_p) \right. \right. \\ \left. \left. + \hat{z}_0^k \cos(-\alpha_{ab}^0 + \omega_y p T_p) \cos(\phi_{ab}^0 + \omega_x p T_p) \right) \right) \end{aligned} \quad (10)$$



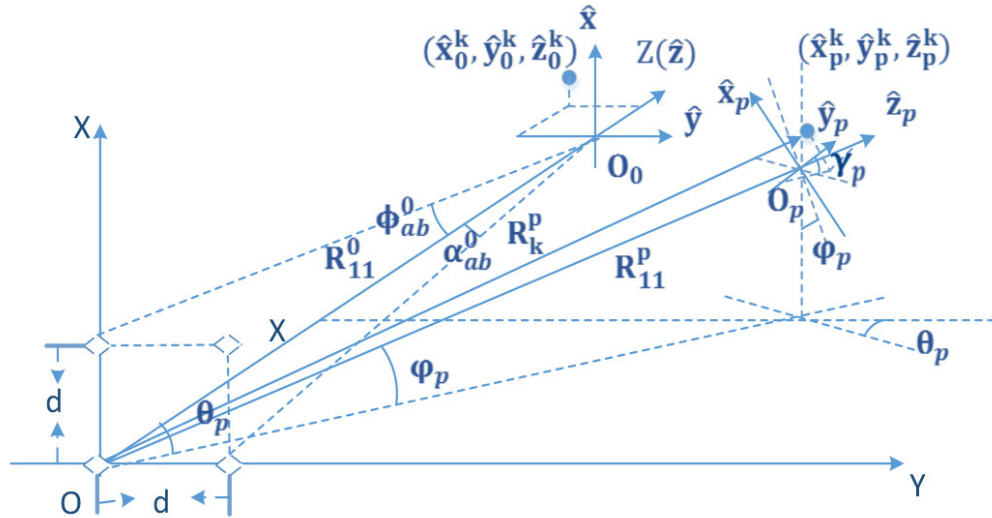


Fig. 4. Motion of the target.

where  $\varphi_p = \omega_x p T_p$  and  $\theta_p = \omega_y p T_p$  (uniform rotation) because of the limited imaging time and  $\omega_x$  and  $\omega_y$  are the rotation angular velocities of the target in the corresponding directions. Since the values of  $\phi_{ab}^0 \pm \omega_x p T_p$ ,  $\alpha_{ab}^0 \pm \omega_y p T_p$ ,  $\phi_{ab}^0$ , and  $\alpha_{ab}^0$  are very small in general, we can make the following transforms consequently:

$$\begin{aligned} \phi_{ab}^0 &\approx \sin(\phi_{ab}^0) \approx \tan(\phi_{ab}^0) \\ &= \frac{X_a}{\sqrt{(R_{11}^0)^2 + (Y_b)^2}} \approx \frac{X_a}{R_{11}^0} \\ &= \frac{(a-1)d}{R_{11}^0} \end{aligned} \quad (11)$$

$$\begin{aligned} \alpha_{ab}^0 &\approx \sin(\alpha_{ab}^0) \approx \tan(\alpha_{ab}^0) \\ &= \frac{Y_b}{\sqrt{(R_{11}^0)^2 + (X_a)^2}} \approx \frac{Y_b}{R_{11}^0} \\ &= \frac{(b-1)d}{R_{11}^0}. \end{aligned} \quad (12)$$

At the same time, let  $a' = a - 1 - (\omega_x p T_p R_{11}^0 / d)$  and  $b' = b - 1 + (\omega_y p T_p R_{11}^0 / d)$ , we can obtain that during any  $p$ th pulse interval, the signal received by the equivalent transceiver at  $(X_a, Y_b)$  can be expressed as

$$\begin{aligned} \tilde{s}_{abp}(t) &\approx \sum_k a_k r_m \left( t - \frac{2R_k}{c} \right) \\ &\cdot \exp \left( -j \frac{4\pi f_c}{c} \left( \hat{x}_0^k \frac{a'd}{R_{11}^0} - \hat{y}_0^k \frac{b'd}{R_{11}^0} + \hat{z}_0^k \right) \right). \end{aligned} \quad (13)$$

This means that by taking the Fourier transform with respect to  $a'$  and  $b'$ , we can obtain the values of  $\hat{x}_0^k$  and  $\hat{y}_0^k$ . Combined with the range information  $R_k$  obtained through the envelopes, we can obtain the 3-D information about the target and realize the 3-D imaging of it by the MIMO radar system at any single pulse interval, namely, through a single snapshot.

Let  $\psi_{abk} = -(4\pi f_c / c) (\hat{x}_0^k (a'd / R_{11}^0) - \hat{y}_0^k (b'd / R_{11}^0) + \hat{z}_0^k)$ , then we can obtain the phase change in the  $x$ -direction by computing the partial derivative of  $a'$  as follows:

$$\Delta \psi_x = \frac{d\psi_{abk}}{da'} = \frac{4\pi f_c d}{c R_{11}^0} \hat{x}_0^k. \quad (14)$$

It is assumed that the distance between two scattering centers in the  $x$ -direction is  $\Delta x$ , and the total number of echoes from them is  $M_1 N_1$ ; then, the total phase difference can be expressed as

$$\psi_x = \frac{4\pi f_c d}{c R_{11}^0} \Delta x (M_1 N_1 - 1). \quad (15)$$

Since the scatterers can be separated when the condition of  $\psi_x \geq 2\pi$  is satisfied, we can obtain the resolution in the  $x$ -direction as

$$p_x = \Delta x_{\min} = \frac{c R_{11}^0}{2df_c (M_1 N_1 - 1)}. \quad (16)$$

Similarly, we can obtain the resolution at the  $y$ -direction as

$$p_y = \Delta y_{\min} = \frac{c R_{11}^0}{2df_c (M_2 N_2 - 1)}. \quad (17)$$

It is easy to see that a high-resolution 2-D image can be obtained with high values of  $M_1 N_1$  and  $M_2 N_2$ . Therefore, we can obtain an image with high resolution by increasing the number of transmitters and receivers. However, this will increase the computational load at the same time.

### III. COMBINATION OF THE MIMO RADAR SYSTEM AND ISAR TECHNIQUE

In Section II, we introduced the principle of 3-D imaging using the MIMO radar system through one snapshot. It is clear to see that although the imaging results will not be affected by motion of the target, and therefore the process of motion compensation is avoided, the computational load will be greatly increased due to the type of imaging technique. Therefore, in this paper, we consider introducing the ISAR imaging technique to the 3-D MIMO imaging for the purpose of using the time samples to replace the space samples so that the number of antenna elements can be reduced. In [22] and [31], the ways of combining the MIMO radar system and the ISAR imaging technique have been discussed in detail. In [22], the aim of using the multiple ISAR images obtained by the receivers is to improve the SNR so that the scatterers could be extracted more easily, but the computational load cannot be reduced when high-resolution imaging

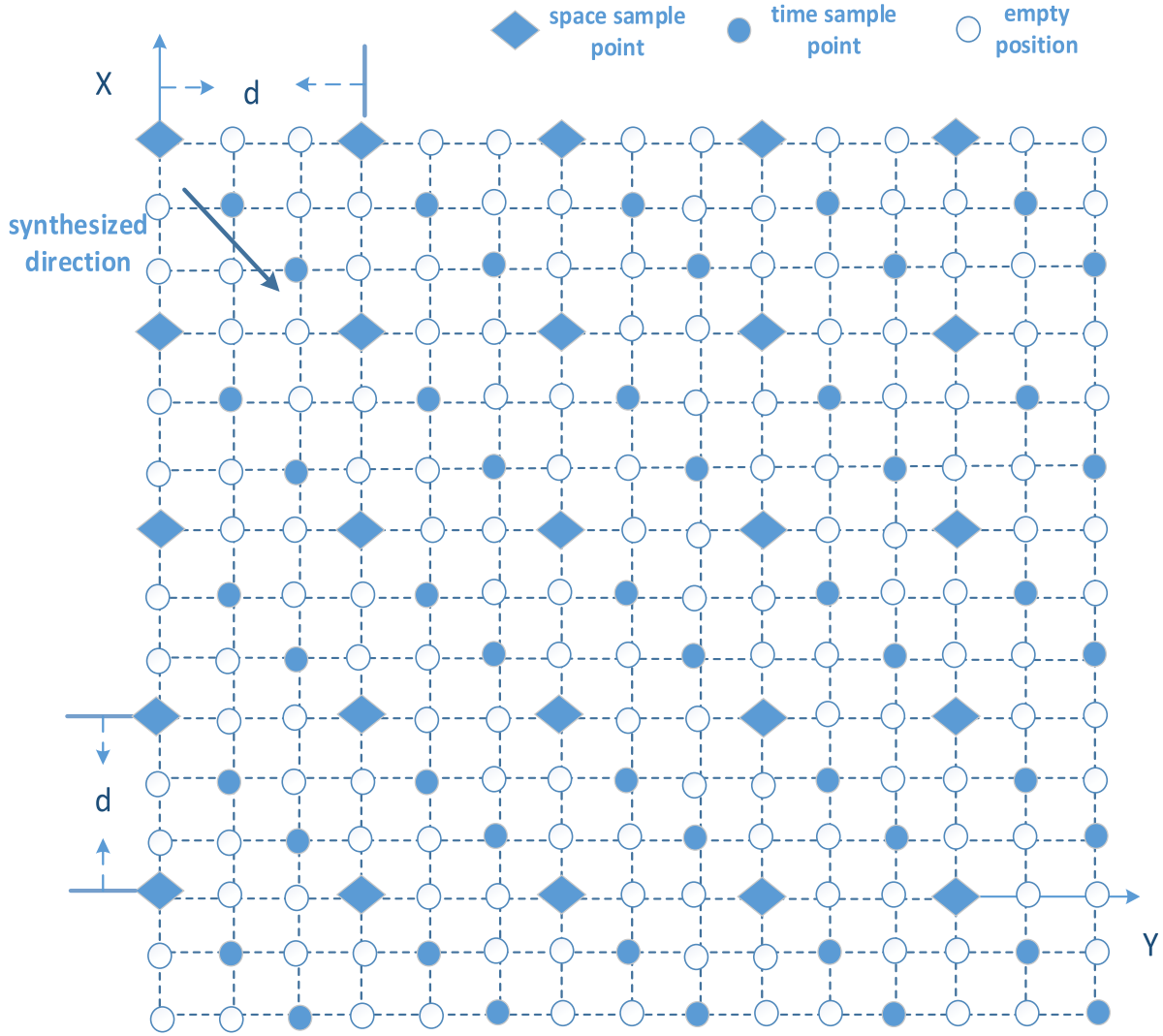


Fig. 5. Arrangement in the synthesized direction.

results are needed. In [31], the ISAR technique was used in the MIMO radar system to improve the imaging resolution, but the accuracy of choosing the imaging time for each equivalent transceiver should be improved because the time samples near a joining position of the signals received by different virtual transceivers are not arranged uniformly, even with the help of the interpolation process.

In this paper, referring to the way shown in [30], a novel method is proposed by combining the ISAR technique and the MIMO radar system to yield the 3-D imaging of a target.

First, since the required ISAR imaging time is quite short, as shown in this paper, this means that the values of  $\varphi_{ab}^0 \pm \omega_x p T_p$  and  $\alpha_{ab}^0 \pm \omega_y p T_p$  are very small. Therefore, we can rewrite (10) as follows:

$$\begin{aligned} \bar{S}_{ab}(t) \approx & \sum_k \sum_p a_k r_m \left( t - \frac{2R_k}{c} \right) \\ & \cdot \exp \left( -j \frac{4\pi f_c}{c} (\hat{x}_0^k (\varphi_{ab}^0 + \omega_x p T_p)) \right) \\ & \cdot \exp \left( -j \frac{4\pi f_c}{c} (\hat{y}_0^k (-\alpha_{ab}^0 + \omega_y p T_p) + \hat{z}_0^k) \right). \quad (18) \end{aligned}$$

It should be noted that when we choose  $PT_p$  as the imaging time, where  $P$  is the total number of the pulses. This means that at most another  $(P-1)M_1 N_1 M_2 N_2$  real sample points can be used for the imaging if we adopt the ISAR imaging technique for the MIMO radar system. How to arrange the positions of the extra sample points is the key problem for improving the imaging resolution based on the planar array. From (33), we notice that the direction of target motion, which will play a role in influencing the effectiveness of improving the imaging resolution, is related to both the  $x$ - and  $y$ -directions. If we choose the direction which is synthesized by the components in both the  $x$ - and  $y$ -directions so as to arrange the direction of the extra time samples, as shown in Fig. 5, it will be hard to calculate the regular arrangement between the sample points received by different transceivers, and a lot of empty positions will remain, which can only be supplemented by the estimated data (for example, through the interpolation process) since few relations can be found between the empty positions. However, the estimated data may produce a lot of errors to the imaging results.

Instead, if we choose to arrange the time samples in the  $x$ - or  $y$ -directions as shown in Figs. 6 and 7, it is easy

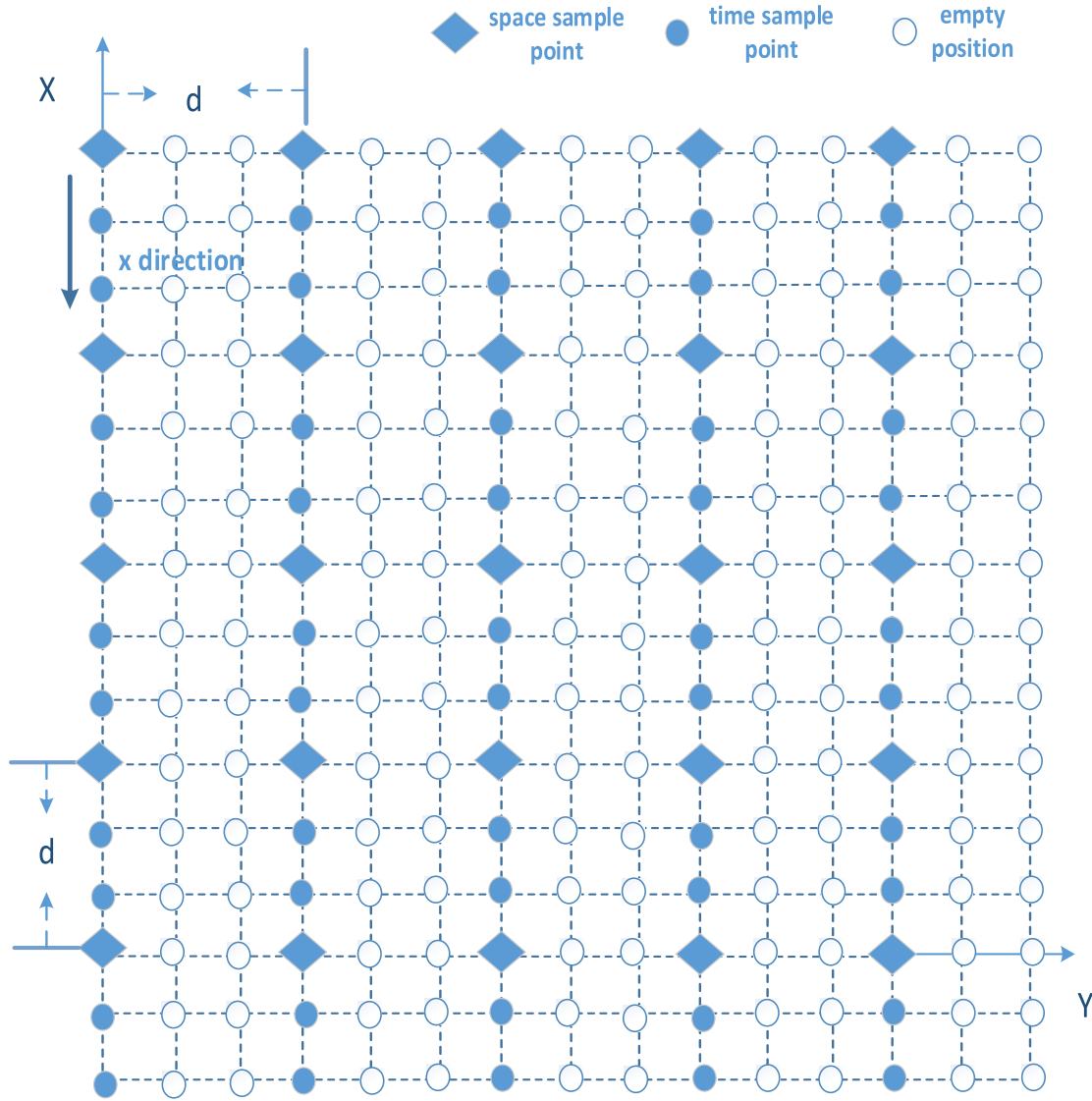


Fig. 6. Arrangement in the  $x$ -direction.

to find that although the number of time samples used is approximately unchanged, the relations between the positions of the spatial sample points, the time sample points, and the empty positions are clear since the time samples and the spatial samples are arranged at the same row or the same column. In this situation, we can obtain the ideal imaging results through some special signal processing technique without introducing the estimated data. This will reduce the errors brought by the false data in the arrangement shown in Fig. 5.

Taking situation 1 in experiment 3 where the square planar array is used as an example. Through calculation, we can obtain that the biggest number of pulses that can be used is 14 if we arrange the time sample points in the diagonal line formed between the adjacent equivalent transmitters because  $d = 7.5$  m, if we arrange the time sample points on the  $x$ - or  $y$ -directions, the number of the time sample points that can be used is 10. From this point, we can find that only four points is not utilized if the time sample points are not arranged in the direction of the diagonal line, which, however, is the direction where the largest number of time sample points can

be used. At the same time, the difficulty of estimating the data in the empty positions between the adjacent transmitters will be largely reduced compared with the situations where the time sample points are arranged in the diagonal line. In other situations using the planar arrays with different length parameters, the numbers of the time sample points that can be arranged on the diagonal line and the longest side of the rectangle formed by the adjacent equivalent transmitters could only be closer with each other.

According to the analysis above, we should either arrange the time sample points in the  $y$ -direction or in the  $x$ -direction. Taking the  $y$ -direction, for example, the relationship between the signals received by different equivalent antenna elements in the same row can be shown in Fig. 8.

According to (12), we can see that the value of  $\alpha_{ab}^0$  only depends on the value of  $Y_b$ , which means that we can extend the same rule to all the rows of the planar array by analyzing how to connect the signals in one row of the planar array. It is assumed that the imaging duration is  $[0, PT_p]$ ; then, the observation angle of the  $k$ th scatterer observed by the  $b$ th

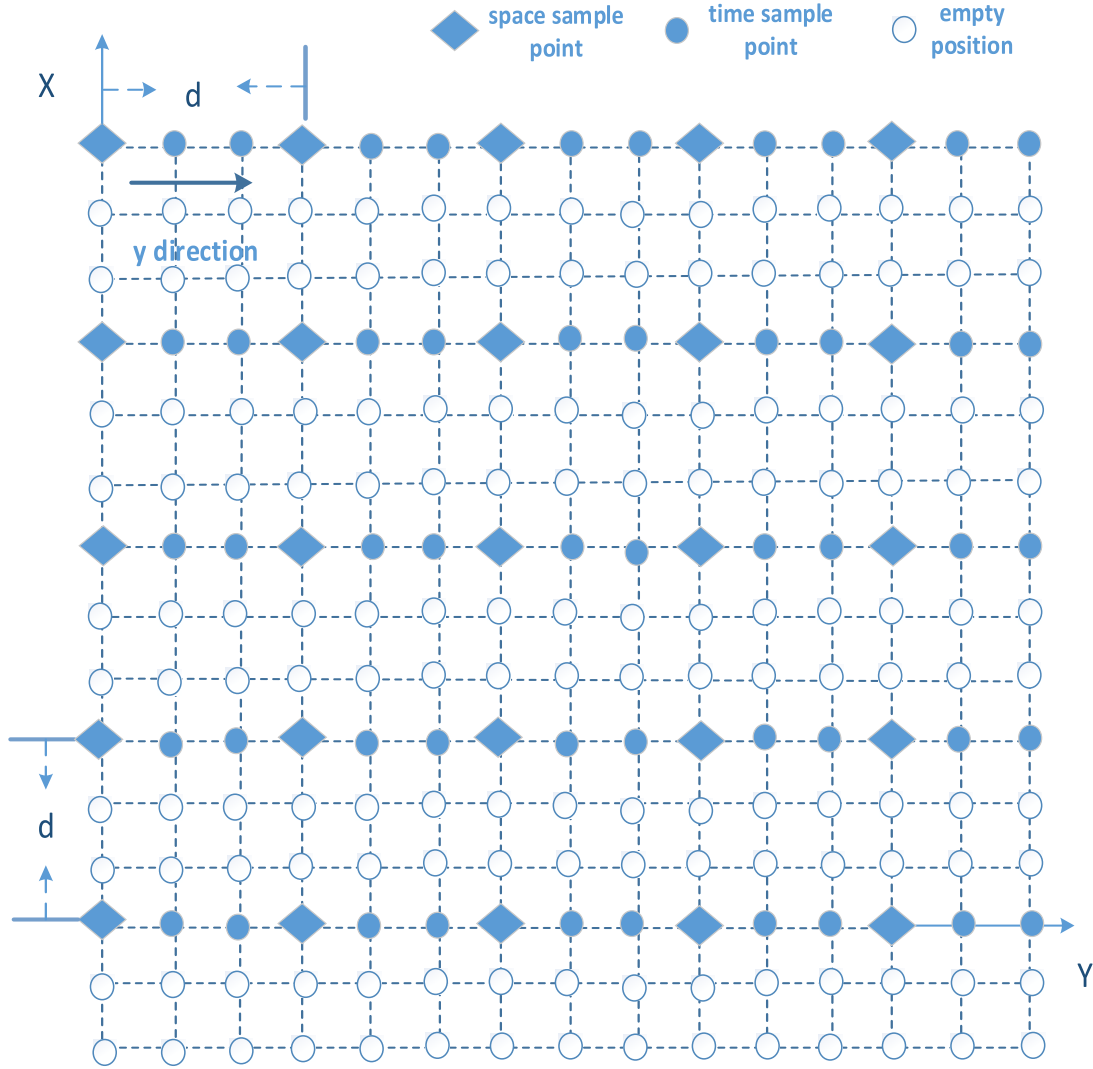


Fig. 7. Arrangement in the y-direction.

equivalent antenna array in the  $a$ th row is

$$\begin{aligned}\Delta\theta_{ab}^k(\text{PT}_p) &= \theta_{ab}^k(\text{PT}_p) - \theta_{ab}^k(0) \\ &= (-\alpha_{ab}^0 + \omega_y \text{PT}_p) - (-\alpha_{ab}^0 + 0) = \omega_y \text{PT}_p.\end{aligned}\quad (19)$$

It is easy to deduce that the global observation angle for the  $k$ th scatterer can be written as

$$\begin{aligned}\Delta\theta_a^k(\text{PT}_p) &= \theta_{a(M_1 N_1)}^k(\text{PT}_p) - \theta_{a1}^k(0) \\ &= (-\alpha_{a(M_1 N_1)}^0 + \omega_y \text{PT}_p) - (-\alpha_{a1}^0 + 0) \\ &= \alpha_{a1}^0 - \alpha_{a(M_1 N_1)}^0 + \omega_y \text{PT}_p.\end{aligned}\quad (20)$$

Besides, if we want to avoid the gaps in the global observation angle, it is demanded that

$$\theta_{a(b-1)}^k(\text{PT}_p) \geq \theta_{ab}^k(0). \quad (21)$$

That is

$$\alpha_{a(b-1)}^0 - \alpha_{ab}^0 \leq \omega_y \text{PT}_p. \quad (22)$$

Since  $\alpha_{a1}^0 - \alpha_{a(M_1 N_1)}^0 \approx \tan(\alpha_{a1}^0 - \alpha_{a(M_1 N_1)}^0) \approx -(d(M_1 N_1 - 1)/R_{11}^0)$ , the resolution in the y-direction can

be rewritten as

$$p_y = \Delta y_{\min} = \frac{c}{2f_c \left( \frac{d(M_1 N_1 - 1)}{R_{11}^0} - \omega_y \text{PT}_p \right)}. \quad (23)$$

As a result, as long as  $\omega_y < 0$ , the value of  $p_y$  will become larger compared with the situation where only the MIMO radar system can be adopted. Of course, for the situation where  $\omega_y > 0$ , as long as we change the observation direction, that is, change the arranged direction of the signals received by different virtual transceivers, the same conclusion can be obtained.

From Fig. 8, it can be found that the time selection process must be introduced when combining the signals from different antenna elements to prevent the observation angles of adjacent antenna elements from being overlapped. In this way, all the time samples can be arranged uniformly. Therefore, we can obtain the combination of signals from the antenna elements in the  $a$ th row as

$$S_{\text{comb}}^a = \sum_b \bar{S}_{ab}(t - t_b) \text{rect}_{T_b}(t - t_b - \Delta t_b) \quad (24)$$



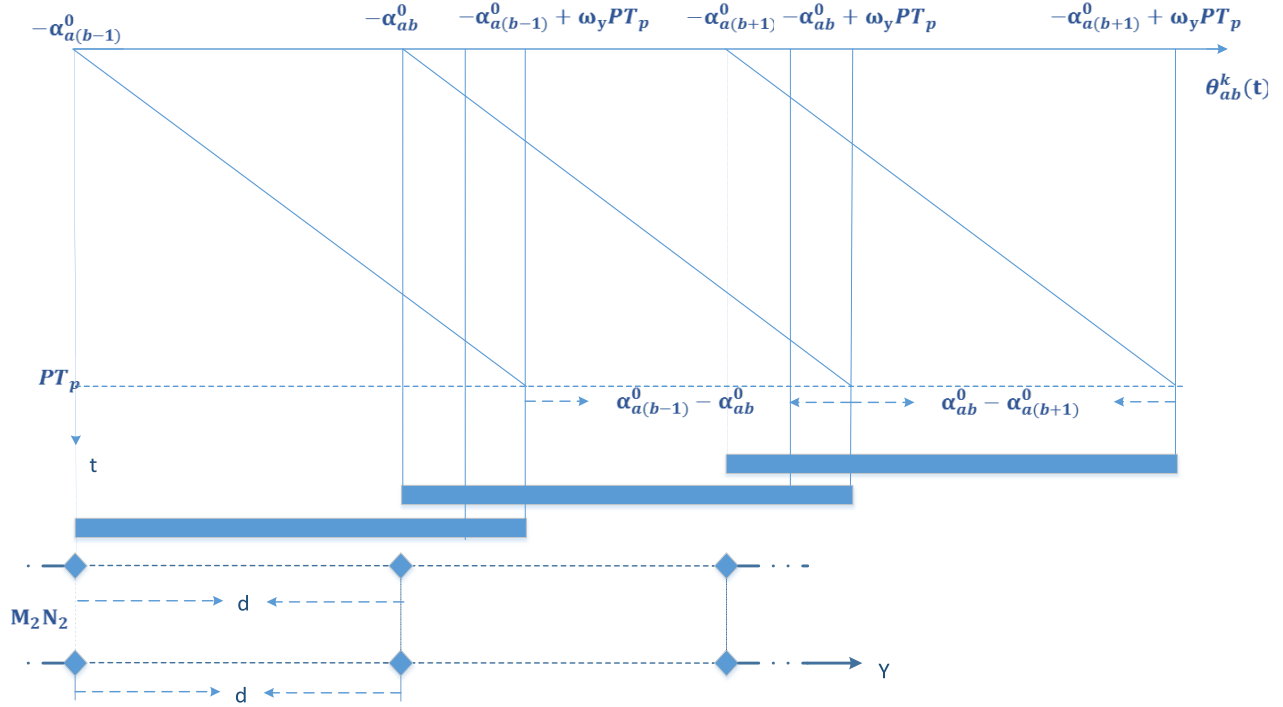


Fig. 8. Total synthetic aperture formed by the MIMO radar system in one row when the observation angles of different antenna elements are overlapped.

where

$$t_b = \frac{(\alpha_{a1}^0 + \alpha_{a(M_1 N_1)}^0)}{2\omega_y} - \frac{\alpha_{ab}^0}{\omega_y}, \quad T_b = \frac{(\alpha_{a(b-1)}^0 + \alpha_{a(b+1)}^0)}{2\omega_y}$$

$$\Delta t_b = \frac{(\alpha_{a(b-1)}^0 + \alpha_{a(b+1)}^0)}{4\omega_y} - \frac{\alpha_{ab}^0}{2\omega_y}, \quad \alpha_{a0}^0 = \alpha_{a1}^0 + \omega_y PT_p$$

and

$$\alpha_{a(M_1 N_1 + 1)}^0 = \alpha_{a(M_1 N_1)}^0 - \omega_y PT_p.$$

In this way, we can get the combined signal of each row in the  $y$ -direction or each column in the  $x$ -direction, and the imaging resolution will be improved in the corresponding direction by connecting the signals received by different transceivers in the same row or column. All the parameters needed in the process can be ascertained through the radar system except for  $\omega_y$ , which must be estimated through the received data. The details of the estimation process will be discussed in Section V. Furthermore, in order to assure high resolution in both directions, the equivalent virtual antenna array is usually designed to be a square, which means that we need to choose a suitable direction (row or column) to arrange the time samples. Generally, if the condition (21) is met in the two directions, it would be fine to arrange the time samples in either direction. Otherwise, it would be better to arrange the time samples in the direction where condition (21) is met or the direction where the estimated angular velocity is bigger when condition (21) cannot be met in the two directions.

#### IV. IMAGING PROCESS BASED ON 2-D CS TECHNIQUE

In practical applications, the length of the signal received by each antenna element is uncertain. It is quite possible that

there will be gaps between the observation angles of different elements, as shown in Fig. 9. In [31] and [32], an interpolation process was used to solve the problem, and the performance would be affected in a way due to the complex motion of the target and the lack of regulations of the signals. Hence, the estimated data obtained by the interpolation process may deviate from the supposed data and the imaging result would be affected.

Here, as an alternate way, we try to use the knowledge of CS techniques to solve the problem. Since the target is usually composed of only a few strong scatterers that are often sparsely distributed, as an effective sparse signal recovery algorithm, CS can be used to improve the imaging resolution. Besides, when the data are incomplete, the adoption of CS can also help to solve the problem, which means that even in the situation where some data are lost in the echoes, the images with high quality can still be obtained through the type of sparse signal recovery technique. Back to the situation in this paper, the gaps between the adjacent observation angles can be seen as the loss of space samples in the corresponding positions. As a result, if we use the CS technique instead of the Fourier transform to deal with the combined signal in the  $y$ -direction, fine resolution in the  $y$ -direction can still be obtained. Therefore, images with high quality through the combination of the ISAR technique and the MIMO radar system can be obtained without introducing the estimated data when there are gaps in the global observation angle. Of course, this type of technique still can be applied when there are no gaps between the adjacent observation angles. Since the CS technique can improve the resolution of the images with a limited number of the echoes, it can also help to reduce the

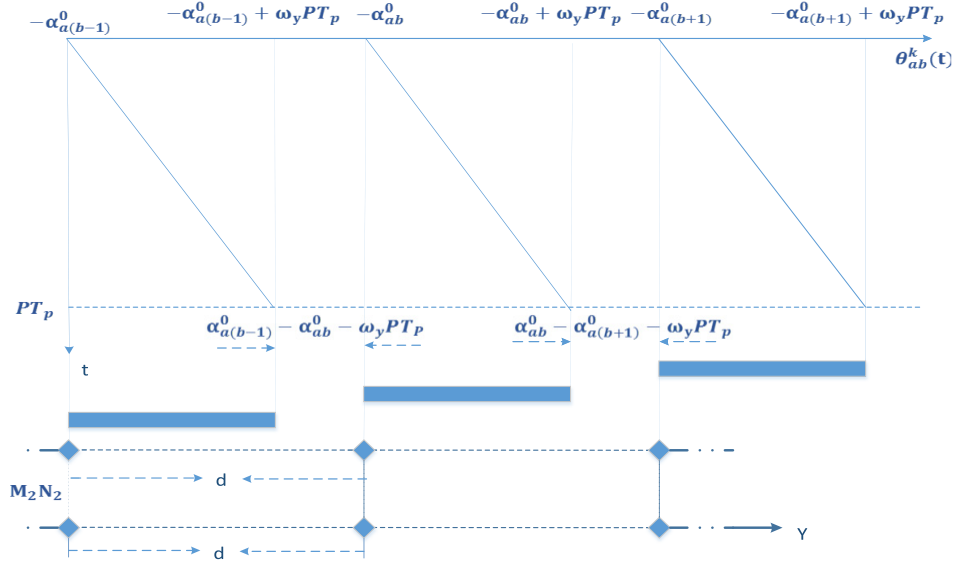


Fig. 9. Total synthetic aperture formed by the MIMO radar system in one row when there are gaps between the observation angles of different elements.

computational complexity. Furthermore, it is easy to see that the 2-D signal can be arranged to have the same structure in two directions. As a result, we can adopt similar measures in two directions. We still take the configuration in Section II as the example, and it is assumed that the final combined signals obtained can be expressed as

$$S_{\text{comb}} = \sum_a S_{\text{comb}}^a = \sum_a \sum_b \bar{S}_{ab}(t - t_b) \text{rect}_{T_b}(t - t_b - \Delta t_b) \quad (25)$$

where  $S_{\text{comb}}^a$  is the combined 3-D signal in the  $a$ th row which includes the range information of the scatterer in the time domain  $t$ . It is obvious that  $S_{\text{comb}}$  includes the 3-D information about the target, where  $a$  and  $b$  can be regarded as the indices reflecting the 2-D information of the target, and the third dimension information can be reflected in the time domain  $t$  through time delays. For the convenience of analysis, we only take into consideration the 2-D information of  $S_{\text{comb}}$  which includes the sample points of the signals in the  $x$ - and  $y$ -directions at each specific instant, namely, variable  $t$  can be regarded as constant at that moment. Then, by taking similar measurements to the 2-D information at each specific instant, we can obtain the positions of the scatterers in three directions.

Now, fixing variable  $t$ , since it can be regarded as constant at that specific instant, and denoting the discretized form of  $S_{\text{comb}}$  as  $s_c \in C^{M' \times N'}$  (where  $M' = M_1 N_1$ ,  $N'$  is the total number of samples in the row corresponding to the  $y$ -direction,  $N' > M_2 N_2$ ), we can obtain the 2-D image of the target by solving the following optimization problem based on the knowledge of CS:

$$\min \|\alpha\|_p \quad \text{s.t.} \quad s_c = F_1 \alpha F_2^T + \varepsilon \quad (26)$$

where  $\alpha \in C^{P_1 \times P_2}$  is the 2-D image including the information in the  $x$ - and  $y$ -directions,  $\varepsilon$  is the noise matrix,  $\|\alpha\|_p$  is the

$\ell_p$  norm of  $\alpha$  [20],  $N' > M_2 N_2$ ,  $P_1 \geq M'$ ,  $P_2 \geq N'$ , and  $F_1 \in C^{M' \times P_1}$ , and  $F_2 \in C^{N' \times P_2}$  can be seen as the Fourier dictionaries in two directions, and can be defined as

$$\begin{aligned} [F_1]_{m'p_1} &= \exp\left(-j2\pi \frac{m'p_1}{P_1}\right) \\ [F_2]_{n'p_2} &= \exp\left(-j2\pi \frac{n'p_2}{P_2}\right) \end{aligned} \quad (27)$$

where  $m' = 1, 2, \dots, M'$ ,  $n' = 1, 2, \dots, N'$ ,  $p_1 = 1, 2, \dots, P_1$ , and  $p_2 = 1, 2, \dots, P_2$ . From (40), it is obvious that the reason why the knowledge about the CS technique can be applied here is that  $\alpha$  is a sparse representation of the received signal  $s_c$  based on the dictionary matrices  $F_1$  and  $F_2$ . Generally, in order to use the traditional methods in the CS which are designed to process the 1-D signal, it would be a good choice to make the transform as follows:

$$s_c = F_1 \alpha F_2^T + \varepsilon \Leftrightarrow \Phi A = S + E \quad (28)$$

where  $S = \text{vec}(s_c)$ ,  $A = \text{vec}(\alpha)$ ,  $E = \text{vec}(\varepsilon)$ , and  $\Phi = F_2 \otimes F_1$  is the Kronecker product of  $F_2$  and  $F_1$  [39]. However, the problem is that the computation load and the required memory will be greatly increased for the reason that as an underdetermined system of linear equation,  $S = \Phi A$  is too large to be solved. For example, for  $F_1 \in C^{64 \times 128}$  and  $F_2 \in C^{64 \times 128}$ ,  $\Phi$  will have the dimension of  $4096 \times 16384$ . As a result, referring to [40], an algorithm which is designed to directly solve (28) will be applied to reduce the computational load and the memory required by using the traditional algorithms in this paper. Even the most popular algorithms in the CS technique such as sparse Bayes learning (SBL) and SL0 (which have shown much better performance than those of other CS algorithms [20], [38], [48]) are designed for 1-D signals. Hence, they will also face the problems mentioned above.

According to [40], through a modification to the SL0 algorithm provided in [41], the traditional SL0 algorithm designed

for 1-D signal can be transformed to an algorithm which can also be applied to 2-D signals directly. As for the situation in this paper, referring to the method in [40], through replacing  $s$  with  $\alpha$  and the set  $S$  with  $\{\alpha | F_1 \alpha F_2^T = s_c\}$  in the projection step would make the traditional CS algorithm based on SL0 for the 1-D signal suitable for working directly with the 2-D signal in the situation of this paper. That is, according to [40, Ths. 3 and 4], the projection of the matrix  $\alpha'$  onto the feasible set  $\{\alpha | F_1 \alpha F_2^T = s_c\}$  can be given by

$$\alpha = \alpha' - F_1^+ (F_1 \alpha' F_2^T - s_c) F_2^+ \quad (29)$$

where  $F_1^+ = F_1^T (F_1 F_1^T)^{-1}$  and  $F_2^+ = F_2^T (F_2 F_2^T)^{-1}$  are the pseudo inverses of  $F_1$  and  $F_2$ , respectively. The initial solution of  $F_1 \alpha F_2^T = s_c$  can also be expressed as  $\hat{\alpha}_0 = F_1^+ \alpha (F_2^+)^T$ , namely, the minimum  $\ell_2$  norm solution of  $F_1 \alpha F_2^T = s_c$ . Referring to the algorithm in [29], when finding the optimal solution of (26), we can use the continuous function  $F_\sigma(\alpha) \triangleq P_1 P_2 - \sum_i \sum_j \exp(-(a_{ij}^2 / 2\sigma^2))$  as the cost function to replace  $\|\alpha\|_p$  to be minimized, since it approximates the  $\ell_0$  norm of  $\alpha$  ( $\|\alpha\|_0$ ) (which represents the number of elements in  $\alpha$  that are not zeroes, and thus the most optimal solution of (26) among the solutions which have the form  $\|\alpha\|_p$ ), and can be minimized by means of a minimization algorithm for continuous functions, such as the steepest descent method, since  $\|\alpha\|_0$  is not continuous.

As a result, we can obtain the image of the target by solving the following problem:

$$\begin{aligned} \hat{\alpha} &= \lim_{\sigma \rightarrow \sigma_{\min}} \arg \min F_\sigma(\alpha) \\ \text{s.t. } &\|s_c - F_1 \alpha F_2^T\| < \bar{\varepsilon} \end{aligned} \quad (30)$$

where  $\bar{\varepsilon}$  is the variance of  $\varepsilon$  and the algorithm structure for the situation in this paper can be expressed as follows.

Initialization.

1) Let  $\hat{\alpha}_0 = F_1^+ \alpha (F_2^+)^T$ .

2) Choose a suitable decreasing sequence for

$$\sigma, [\sigma_1, \dots, \sigma_J].$$

For  $j = 1, \dots, J$

1) Let  $\sigma = \sigma_j$ .

2) Minimize the function  $F_\sigma(\alpha)$  on the feasible set  $\{\alpha | F_1 \alpha F_2^T = s_c\}$  using  $L$  iterations of the steepest ascent algorithm (followed by projection onto the feasible set).

Initialization:  $\alpha = \hat{\alpha}_{j-1}$

For  $l = 1, \dots, L$  (loop  $L$  times)

a) Let  $\delta$  be the gradient of  $F_\sigma(\alpha)$ .

b) Let  $\alpha \leftarrow \alpha - \mu \delta$ . ( $\mu$  is a small positive constant).

c) Project  $\alpha$  back onto the feasible set

$$\alpha \leftarrow \alpha - F_1^+ (F_1^+ \alpha (F_2^+)^T - s_c) (F_2^+)^T. \quad (31)$$

3) Set  $\hat{\alpha}_j = \alpha$ .

The final answer is  $\hat{\alpha} = \hat{\alpha}_J$ .

When  $\alpha$  is not complete, namely, the values of some rows or some columns of  $\alpha$  are zeroes [in the situation in this paper, it means that (21) is not met], we can use  $F_1' = F_1 E_1$  and  $F_2' = F_2 E_2$  to replace  $F_1$  and  $F_2$ , where  $E_1$  and  $E_2$  are the unit matrixes whose corresponding rows to  $\alpha$  have been set to zeroes for the purpose of ensuring the reconstructed  $\alpha$  will not be affected by incomplete data. What should be

noted is that if the data are complete, the 2-D CS recovery algorithm will show better results compared with those of the incomplete data when  $P_1$  and  $P_2$  are increased. Since the algorithm is designed based on the SL0 method for the 1-D signals, we can also make some improvements based on the real conditions by changing the cost function  $F_\sigma(\alpha)$ , which has been tried for the 1-D signals. Ma *et al.* [20] changed  $F_\sigma(\alpha)$  to the combination of the first-order negative exponential function and the total variation function in order to get better results in the specific situations where the target has a flat patch facing the radar, and the gradient of the reflectivity has high values at the edge of the flat patch surface. Of course, we can use a diagonal loading method [42] and the singular value decomposition method [20], during the process of calculating the pseudoinverses of  $F_1'$  and  $F_2'$  to assure a robust implementation of the algorithm in case  $F_1' F_1'^T$  and  $F_2' F_2'^T$  are ill-conditioned.

Then, we can obtain the 2-D information of the scatterers on the target with the value of  $\alpha$ , and combined with the information in the range direction, we can reconstruct the coordinates of the scatterers in space.

## V. RANGE ALIGNMENT AND VELOCITY ESTIMATION

As described in Section II, the relative time delays between different transmitters and receivers are always larger than the range resolution. Therefore, we must align the envelopes of the received signals before more operations can be implemented to the signals, and so that the range information obtained from the signals transmitted by different antenna elements and received by different receivers can be equivalent for the same scatterer. Besides, if we want to obtain the combined signal using the algorithm described in Section III, the knowledge of  $\omega_x$  and  $\omega_y$  must be determined before the combination can be done, which means that the parameters must be estimated through the received data. Next, we will make an explicit description of the two processes. (What should be noted is that we use the same way as in [22] to implement the phase compensation.)

### A. Range Alignment

The process of range alignment for the situation where the MIMO radar system configuration and the ISAR technique are both applied can be described as follows: the first step is the internal range alignment for the signal received by each antenna element, where the shifts of the ranges are caused by different time delays related to the sequence of pulses, which is indifferent compared with the situations in the usual 2-D ISAR imaging process. Hence, we can apply here the standard methods for the range alignment for the ISAR imaging technique such as the envelope correlation method [43] and the dominant scatterer method [44]. After the first step of the range alignment, we can rewrite (1) as

$$\begin{aligned} S_{mn}(t) &= \sum_k \sum_p \alpha_k r_m \left( t - t_0 - \frac{R_{m0k}^t + R_{n0k}^r}{c} \right) \\ &\quad \cdot \exp \left( -j \frac{2\pi f_c}{c} (R_{mpk}^t + R_{npk}^r) \right) \end{aligned} \quad (32)$$

where  $t_0$  can be seen as the equivalent time delay obtained for all the signals received by the same transceiver after the internal range alignment process of the first step. Then, from (32), it is easy to see that the time shifts between the signals received by different transceivers are mainly caused by  $R_{m0k}^t$  and  $R_{n0k}^r$ , which, however, have nothing to do with the ordinal number of pulses  $p$  after the first step of the range alignment. Now, different time delays caused by the differences between various positions of the transmitters and the receivers become the only resources that cause the time shifts of the envelopes from the same scatterer received by different receivers. Now, we try to eliminate the effects brought by the differences of the positions. According to the geometric relations between the target and the radar system,  $R_{m0k}^t$  and  $R_{n0k}^r$  can be expressed as

$$\begin{aligned} R_{m0k}^t &= \sqrt{(x_m - x_0^k)^2 + (y_m - y_0^k)^2 + (z_0^k)^2} \\ &= \sqrt{(x_m)^2 - 2x_mx_0^k + (y_m)^2 - 2y_my_0^k + (R_0^k)^2} \end{aligned} \quad (33)$$

where  $x_m = m_1d_t + u_{r0}$  and  $y_m = m_2d_t + v_{r0}$ . The  $R_{n0k}^r$  has the same form of  $R_{m0k}^t$  in (33) by replacing variable  $m$  with  $n$  and  $t$  with  $r$ , and  $x_n = n_1d_r + u_{r0}$ ,  $y_n = n_2d_r + v_{r0}$ .

$(R_0^k)^2 = (x_0^k)^2 + (y_0^k)^2 + (z_0^k)^2$  and  $(x_0^k, y_0^k, z_0^k)$  is the coordinate of the  $k$ th scatterer in the coordinate system  $(O, X, Y, Z)$ .  $x_0^k = X_0 + \hat{x}_0^k$ ,  $y_0^k = Y_0 + \hat{y}_0^k$ ,  $z_0^k = Z_0 + \hat{z}_0^k$ , and  $(X_0, Y_0, Z_0)$  is the coordinate of  $O_0$  in the coordinate system  $(O, X, Y, Z)$  and  $(R_0)^2 = (X_0)^2 + (Y_0)^2 + (Z_0)^2$ .

Since  $x_m$ ,  $y_m$ ,  $x_n$ , and  $y_n$  are far smaller than  $R_0^k$ , we can make a 2-D Taylor expansion to  $R_{m0k}^t$  with  $x_m$  and  $y_m$  at the near zero value and  $R_{n0k}^r$  with  $x_n$  and  $y_n$  at the near zero value, respectively. Then, by keeping three terms of the expansion results, we can obtain

$$\begin{aligned} R_{m0k}^t &\approx R_0^k - \frac{x_mx_0^k + y_my_0^k}{R_0^k} \\ &\quad + \frac{1}{2}(x_m)^2 \left( \frac{1}{R_0^k} - \frac{(x_0^k)^2}{(R_0^k)^3} \right) \\ &\quad + \frac{1}{2}(y_m)^2 \left( \frac{1}{R_0^k} - \frac{(y_0^k)^2}{(R_0^k)^3} \right) - x_my_m \frac{x_0^ky_0^k}{(R_0^k)^3}. \end{aligned} \quad (34)$$

Then, the  $R_{n0k}^r$  has the same form of  $R_{m0k}^t$  in (34) by replacing the variable  $m$  with  $n$  and  $t$  with  $r$ .

Since  $R_0^k \approx R_0$ ,  $x_0^k \approx X_0$ , and  $y_0^k \approx Y_0$ , we can rewrite (34) for the far field condition as follows:

$$\begin{aligned} R_{m0k}^t &\approx R_0^k - \frac{x_mX_0 + y_mY_0}{R_0} \\ &\quad + \frac{1}{2}(x_m)^2 \left( \frac{1}{R_0} - \frac{(X_0)^2}{(R_0)^3} \right) \\ &\quad + \frac{1}{2}(y_m)^2 \left( \frac{1}{R_0} - \frac{(Y_0)^2}{(R_0)^3} \right) - x_my_m \frac{X_0Y_0}{(R_0)^3}. \end{aligned} \quad (35)$$

Then, the  $R_{n0k}^r$  has the same form of  $R_{m0k}^t$  in (35) by replacing the variable  $m$  with  $n$  and  $t$  with  $r$ .

Hence, we can construct the range adjustment function as

$$\begin{aligned} R_{\text{adj}} &\approx \frac{(x_m + x_n)X_0 + (y_m + y_n)Y_0}{R_0} \\ &\quad - \frac{1}{2}((x_m)^2 + (x_n)^2) \left( \frac{1}{R_0} - \frac{(X_0)^2}{(R_0)^3} \right) \\ &\quad - \frac{1}{2}((y_m)^2 + (y_n)^2) \left( \frac{1}{R_0} - \frac{(Y_0)^2}{(R_0)^3} \right) \\ &\quad + (x_my_m + x_ny_n) \frac{X_0Y_0}{(R_0)^3}. \end{aligned} \quad (36)$$

Through eliminating the time shifting differences in the envelopes caused by different positions by adding the range adjustment function to the corresponding component of the received signals, we can make the time delays in the signals received by different transceivers the same, and thus accurate information on the target in the range direction can be obtained by making suitable transformations to the envelopes of the received signals.

As  $R_{m0k}^t + R_{n0k}^r + R_{\text{adj}} = 2R_0^k$ , after range adjustment, we can obtain

$$\begin{aligned} \tilde{S}_{mn}(t) &= \sum_k \sum_p \alpha_k r_m \left( t - t_0 - \frac{R_{m0k}^t + R_{n0k}^r + R_{\text{adj}}}{c} \right) \\ &\quad \cdot \exp \left( -j \frac{2\pi f_c}{c} (R_{mpk}^t + R_{npk}^r) \right) \\ &= \sum_k \sum_p \alpha_k r_m \left( t - \frac{2R_k}{c} \right) \\ &\quad \cdot \exp \left( -j \frac{2\pi f_c}{c} (R_{mpk}^t + R_{npk}^r) \right) \end{aligned} \quad (37)$$

where  $R_k = R_0^k + (ct_0/2)$ . Since the phase change in the frequency domain corresponds to the time shift in the time domain, the whole process of range alignment can be realized in the frequency domain.

### B. Velocity Estimation

In [31] and [45]–[47], some algorithms have been provided to estimate the rotation parameters in different situations. Since they are all designed for specific situations, the algorithms may not give ideal performance when applied to the configuration in this paper. Hence, considering the characteristics of the configuration designed in this paper, we provide a relatively novel parameter estimation method which is quite suitable for the situation where the imaging time is short, the target is moving in the far field and there exist dominant scatterers in the target.

In Section II, we assume that the target moves at a uniform velocity during the imaging time, and therefore, we suppose that the angular velocity is a constant. However, in reality, changes in  $\varphi_p(pT_p)$  and  $\theta_p(pT_p)$  are more likely to be approximated to

$$\varphi_p(pT_p) = \varphi_p^0(pT_p) + \frac{1}{2}\beta(pT_p)^2. \quad (38)$$

$\theta_p(pT_p)$  has the same form of (38) by replacing the variables  $\phi$  and  $\beta$  with  $\theta$  and  $\gamma$ , respectively.  $\varphi_p^0$  and  $\theta_p^0$  are the first-order coefficients of  $\varphi_p(pT_p)$  and  $\theta_p(pT_p)$ , and  $\beta$  and  $\gamma$



are the second-order coefficients of  $\varphi_p(pT_p)$  and  $\theta_p(pT_p)$ , respectively.

Since the imaging time required in the configuration is very short, we can still consider that  $\varphi_p(pT_p)$  and  $\theta_p(pT_p)$  will change uniformly according to the time at the equivalent angular velocity  $\omega_x$  and  $\omega_y$ , respectively, and the equivalent angular velocities can be calculated as follows when the total imaging time is  $PT_p$ :

$$\omega_x = \varphi_p^0 + \frac{1}{2}\beta PT_p. \quad (39)$$

$\omega_y$  has the same form of (39) by replacing the variables  $\phi$  and  $\beta$  with  $\theta$  and  $\gamma$ , respectively.

Then, it can be seen that as long as we obtain the values of  $\varphi_p^0$ ,  $\theta_p^0$ ,  $\beta$ , and  $\gamma$ , we can obtain estimated values for  $\omega_x$  and  $\omega_y$ . Substitute (38) into (10), during any  $p$ th pulse interval, the signal received by the equivalent transceiver at  $(X_a, Y_b)$  can be expressed (40), as shown at the bottom of the next page.

For every row,  $a$  can be regarded as a constant, so we can obtain (41), as shown at the bottom of the next page.

Since

$$\cos(\theta_p(pT_p)) \approx 1 \quad (42)$$

$$\cos(-\alpha_{ab}^0) \approx 1 \quad (43)$$

$$\sin(\theta_p(pT_p)) \approx \theta_p(pT_p) \quad (44)$$

$$\sin(-\alpha_{ab}^0) \approx -\alpha_{ab}^0. \quad (45)$$

Extracting echoes of the dominant scatterer  $k'$  for each equivalent transceiver, we can obtain (46), as shown at the bottom of the next page.

Since  $\cos(\varphi_{ab}^0 + \varphi_p(pT_p)) \approx 1$ , let

$$\begin{aligned} \tilde{S}_p^{k'} &= \tilde{S}_{abp}^{k'} (\tilde{S}_{a(b+1)p}^{k'})^* = (\alpha_{k'})^2 \left( r_m \left( t - \frac{2R_{k'}}{c} \right) \right)^2 \\ &\times \exp \left( -j \frac{4\pi f_c}{c} (-\alpha_{ab}^0 + \alpha_{a(b+1)}^0) \right. \\ &\times \left. \left( \hat{y}_0^{k'} - \hat{z}_0^{k'} \theta_p^0 t T_p - \frac{1}{2} \hat{z}_0^{k'} \gamma (pT_p)^2 \right) \right). \end{aligned} \quad (47)$$

Considering  $\alpha_{a(b+1)}^0 - \alpha_{ab}^0 = (bd/R_{11}^0) - ((b-1)d/R_{11}^0) = (d/R_{11}^0)$ , we can rewrite (52) as

$$\begin{aligned} \tilde{S}_p^{k'} &= (\alpha_{k'})^2 \left( r_m \left( t - \frac{2R_{k'}}{c} \right) \right)^2 \\ &\times \exp \left( -j \frac{4\pi f_c d}{c R_{11}^0} \left( \hat{y}_0^{k'} - \hat{z}_0^{k'} \theta_p^0 t T_p - \frac{1}{2} \hat{z}_0^{k'} \gamma (pT_p)^2 \right) \right). \end{aligned} \quad (48)$$

Therefore, the parameter estimation process can be regarded as the problem in the following:

$$(g, h) = \arg \max_{g, h} \left| \int \tilde{S}_p^{k'} \exp(-j2\pi(g(pT_p) + h(pT_p)^2)) d(pT_p) \right| \quad (49)$$

where  $g = -(2f_c d \theta_p^0 / c R_{11}^0)$ ,  $h = (f_c d \gamma / c R_{11}^0)$ . For convenience, we can calculate the value of  $g$  by the Fourier transform. Furthermore, in order to get more accurate solutions,

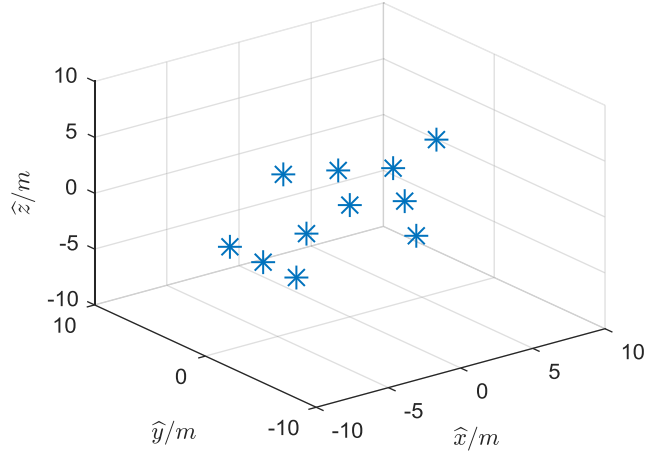


Fig. 10. 3-D model of the target in experiment 1.

we can calculate the values of  $g$  and  $h$  of multiple times by changing the value of  $b$ , and take the mean value of them as the final solution. As a result, we can get  $\theta_p^0$  and  $\gamma$  by calculating

$$\theta_p^0 = -\frac{gcR_{11}^0}{2f_c d}, \quad \gamma = \frac{hcR_{11}^0}{f_c d}. \quad (50)$$

The values of  $\varphi_p^0$  and  $\beta$  can be obtained in the same way. It should be noted that the premise of the estimation method is that there exists a dominant scatterer on the target, and the target is moving in the far field. In other situations, the readers may refer to the estimation methods mentioned in [22] and [47]. What should be mentioned is that if the velocity is not estimated correctly, it may prevent the signals received by different transceivers being combined correctly. As a result, the scatterers in the 2-D images may not be separated very well, which may introduce false scatterers to the final 3-D reconstruction of the target.

## VI. EXPERIMENTAL RESULTS

All the images are the direct imaging results obtained through using the “imagesc” function in MATLAB to the final computation results without any special scaling process.

### A. Experiment 1: Range Alignment

The purpose of the first experiment is to prove that the range alignment algorithm designed in this paper is effective enough for correcting the time shifts between different envelopes. The system parameters are set as follows.

Besides, we describe the moving state of the target as  $(v \cos(\alpha^*) \sin(\theta^*), v \cos(\alpha^*) \sin(\theta^*), v \sin(\alpha^*))$ , where  $v$  is the value of the target velocity and  $\alpha^*$  and  $\theta^*$  are the angles the target moving relative to the  $z$ -axis and the  $y$ -axis.

The 3-D model of the target is shown in Fig. 10, and the antenna array is shown in Fig. 11, where the red points represent the transmitters, the blue points represent the receivers, and the purple points represent the equivalent transceivers. The initial position of the target in the coordinate system  $(O, X, Y, Z)$  is  $(0, 0, 10000 \text{ m})$ .  $v = -300 \text{ m/s}$ ,  $\alpha^* = 0$ , and  $\theta^* = \pi/3$ . In order to better illustrate the effectiveness of the

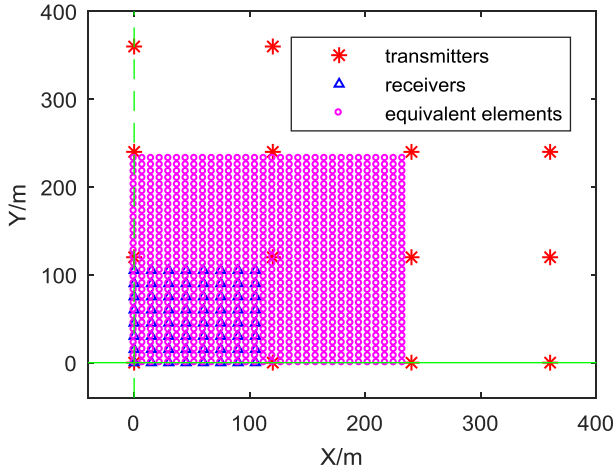


Fig. 11. Antenna array in experiment 1.

algorithm for the range alignment designed in this experiment, we choose  $M_1 = M_2 = 4$ ,  $N_1 = N_2 = 8$ ,  $d_t = N_2 d_r = 120$  m, and  $u_{t0} = v_{t0} = u_{r0} = v_{r0} = 0$ . The imaging time is 0.025 s ( $P = 10$ ).

The results before and after the range alignment are shown in Figs. 12 and 13, respectively, where the  $x$ -axis (labeled as “range units”) represents time samples of the range direction, thus, reflects the time delays of different envelopes, and the  $y$ -axis (labeled as “cross-range units”) represents the combination of the signal pulses of each transceiver, which can also be regarded as amalgamation of time samples and spatial samples. The aim of the experiment is to show that after the range alignment, all the envelopes of the pulses received by different transceivers can be aligned without any time shifts. As a result, it could be seen that in Fig. 12, except for the time shifts between different signals received by the same equivalent transceiver, there is also bigger integral time shifts between the sets of signals received by different transceivers.

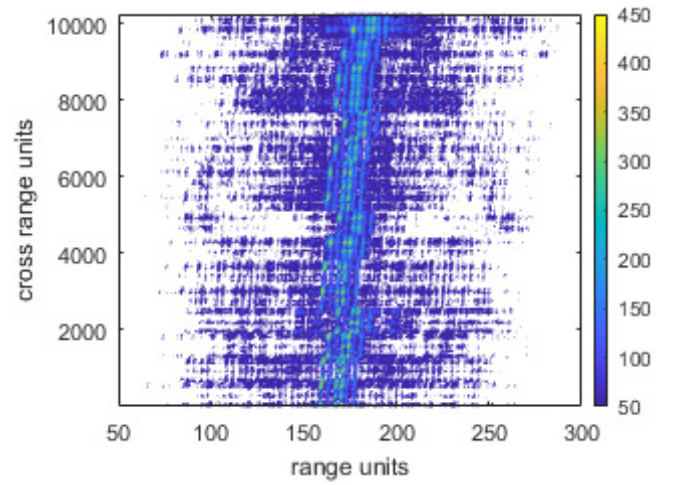


Fig. 12. Envelope before range alignment.

After the process of range alignment, the two kinds of time shifts are adjusted, as shown in Fig. 13.

### B. Experiment 2: Linear Array

In this experiment, we choose  $M_2 = N_2 = 1$ . Under such a condition, the planar array would become a linear array, and as a result, the effectiveness of the algorithm proposed in this paper could be better substantiated by making a comparison with the results using the algorithm designed in [31]. Since the antenna array has become now linear, only 2-D images can be obtained by extracting information in the cross-range direction and the range direction. Here we still use the same system parameters shown in Table I, and the target has the same velocity and the same direction of motion as experiment 1, but the size of the target model adopted will be set as 2/3 of the one in experiment 1 in order to better prove the advantages of the algorithm designed in this paper.

$$\tilde{S}_{abp}(t) = \sum_k \alpha_k r_m \left( t - \frac{2R_k}{c} \right) \cdot \exp \left( -j \frac{4\pi f_c}{c} (\hat{x}_0^k \sin(\varphi_{ab}^0 + \phi_p(pT_p)) + \hat{y}_0^k \sin(-\alpha_{ab}^0 + \theta_p(pT_p)) \right. \\ \left. \times \cos(\varphi_{ab}^0 + \phi_p(pT_p)) + \hat{z}_0^k \cos(-\alpha_{ab}^0 + \theta_p(pT_p)) \cos(\varphi_{ab}^0 + \phi_p(pT_p)) \right). \quad (40)$$

$$\tilde{S}_{abp} = \sum_k \alpha_k r_m \left( t - \frac{2R_k}{c} \right) \exp \left( -j \frac{4\pi f_c}{c} (\hat{x}_0^k \sin(\varphi_{ab}^0 + \phi_p(pT_p)) \right. \\ \left. + \hat{y}_0^k (\sin(-\alpha_{ab}^0) \cos(\theta_p(pT_p)) + \cos(-\alpha_{ab}^0) \sin(\theta_p(pT_p))) \cdot \cos(\varphi_{ab}^0 + \phi_p(pT_p)) \right. \\ \left. + \hat{z}_0^k (\cos(-\alpha_{ab}^0) \cos(\theta_p(pT_p)) - \sin(-\alpha_{ab}^0) \sin(\theta_p(pT_p))) \cos(\varphi_{ab}^0 + \phi_p(pT_p)) \right). \quad (41)$$

$$\tilde{S}_{abp}' \approx \alpha_k' r_m \left( t - \frac{2R_{k'}}{c} \right) \exp \left( -j \frac{4\pi f_c}{c} (\hat{x}_0^{k'} \sin(\varphi_{ab}^0 + \phi_p(pT_p)) + ((\hat{y}_0^{k'} (-\alpha_{ab}^0) + \hat{z}_0^{k'}) \right. \\ \left. + (\hat{y}_0^{k'} + \hat{z}_0^{k'} \alpha_{ab}^0) \theta_p p T_p + \frac{1}{2} (\hat{y}_0^{k'} + \hat{z}_0^{k'} \alpha_{ab}^0) \gamma (pT_p)^2) \cos(\varphi_{ab}^0 + \phi_p(pT_p)) \right). \quad (46)$$

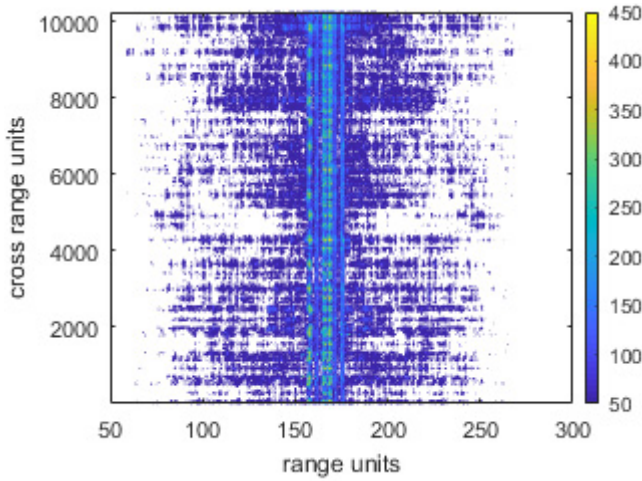


Fig. 13. Envelope after range alignment.

TABLE I  
SYSTEM PARAMETERS

Carrier frequency	10GHz	Pulse repetition frequency	400Hz
Band width	400MHz	Subcode number	120

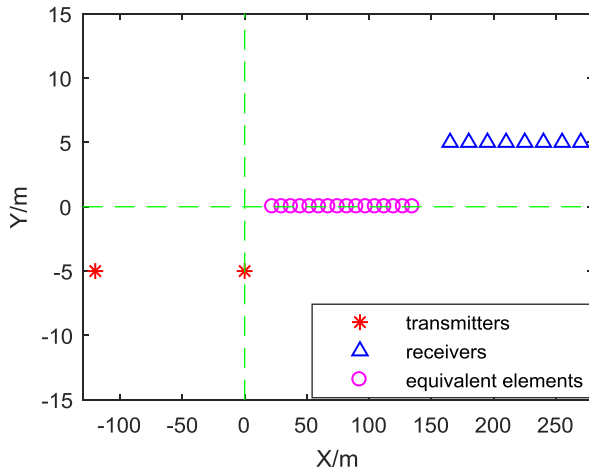


Fig. 14. Antenna array in experiment 2.

1) *Situation 1*: In this situation, the imaging time is 0.1 s ( $P = 40$ ),  $M_1 = 2$ ,  $N_1 = 8$ ,  $d_t = N_1 d_r = 120$  m,  $u_{t0} = -120$  m,  $v_{t0} = -5$  m,  $u_{r0} = 165$  m, and  $v_{r0} = 5$  m. The initial position of the target in the coordinate system ( $O, X, Y, Z$ ) is  $(0, 10000 \text{ m}, 0)$ .  $v = -300$  m/s,  $\alpha^* = 0$ , and  $\theta^* = \pi/2$ . The linear array is shown in Fig. 14, where the red points represent the transmitters, the blue points represent the receivers, and the purple points represent the transceivers. It is easy to find that (21) is met, which means that we must adopt the process of time selection if we want to use the algorithm designed in this paper.

The imaging result only using the MIMO radar system designed in this paper is shown in Fig. 15(a). It is easy to see that the resolution in the cross-range direction is very low for the reason that the number of the antenna elements is limited, and therefore the scatterers which are very close

TABLE II  
IMAGING ENTROPIES OF THREE DIFFERENT ALGORITHMS

	MIMO	MIMO+ISAR without time selection	MIMO+ISAR with time selection
Entropy	15.6247	22.2573	13.4264

to each other in the middle of the target are not separated successfully. Fig. 15(b) shows the imaging result using the method of arranging the time samples in [31]. It could be found that by combining the ISAR technique with the MIMO system, the resolution in the cross-range direction has been improved, and the scatterers in the middle of the target have been roughly separated. However, for the reason that the time samples in the joining positions of the signals received by adjacent equivalent transceivers are not uniform, the scatterers are not separated very well, and the sidelobes are so large that different scatterers are almost connected. Fig. 15(c) shows the imaging results by using the algorithm in this paper. Obviously, introduction of the process of time selection enables the scatterers to be separated very well since the time samples obtained by different antenna elements are arranged uniformly in the global aperture formed by the MIMO radar system.

What is more, the cross-range resolution comparison for the scatterers in the middle of the target is given in Fig. 16, where the blue line, the red line, and the green line represent the results obtained by adopting MIMO radar system only, by the combination of the MIMO radar system and the ISAR technique without time selection, and by the combination of the MIMO radar system and the ISAR technique with time selection, respectively. It is obvious that the resolution is improved by using the algorithm designed in this paper. In order to better evaluate the imaging results under the three different conditions, we calculate the imaging entropy of the 2-D images [48], and the results are shown in Table II. Obviously, the entropy of the image obtained by the algorithm in this paper is smaller assuming that this situation is a true reflection of the information about the target.

2) *Situation 2*: In this situation, the imaging time is 0.04 s ( $P = 16$ )  $\text{CM}_1 = 2$ ,  $N_1 = 4$ ,  $d_t = N_1 d_r = 120$  m,  $u_{t0} = 0$  m,  $v_{t0} = -5$  m,  $u_{r0} = 180$  m, and  $v_{r0} = 5$  m. The initial position of the target in the coordinate system ( $O, X, Y, Z$ ) is  $(0, 10000 \text{ m}, 0)$ .  $v = -300$  m/s,  $\alpha^* = 0$ , and  $\theta^* = \pi/2$ . Under such an MIMO radar configuration, the resolution of the image is too low to reflect the true nature of the target if only the MIMO radar system is applied, since the number of the antenna elements is too small. Fig. 17 gives the imaging result under such an MIMO radar configuration, and it can be seen that the imaging result is totally distorted compared with the real target. As a result, we must adopt the ISAR technique to increase the resolution. According to the magnitude and direction of the target velocity, we find that (21) is not met, which means that we must take some measures to prevent the imaging results from being affected by the gaps between the signals received by different equivalent transceivers. If we try to obtain the imaging results through Fourier transforms under such conditions, there will be a lot of false targets

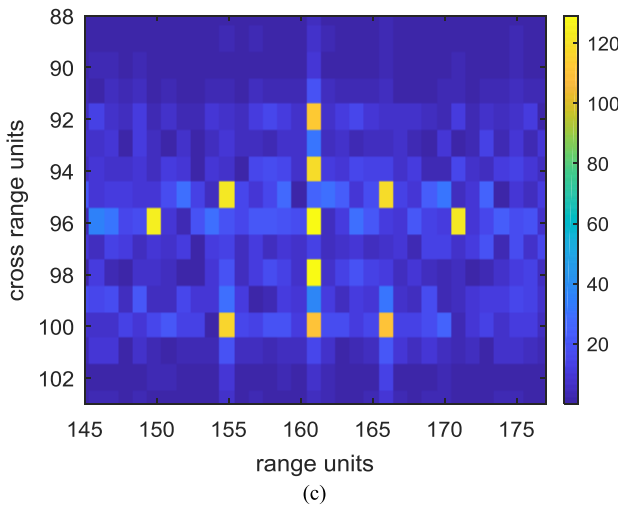
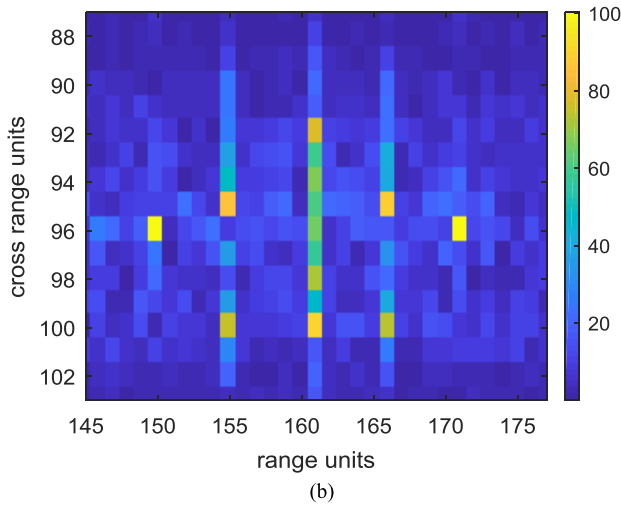
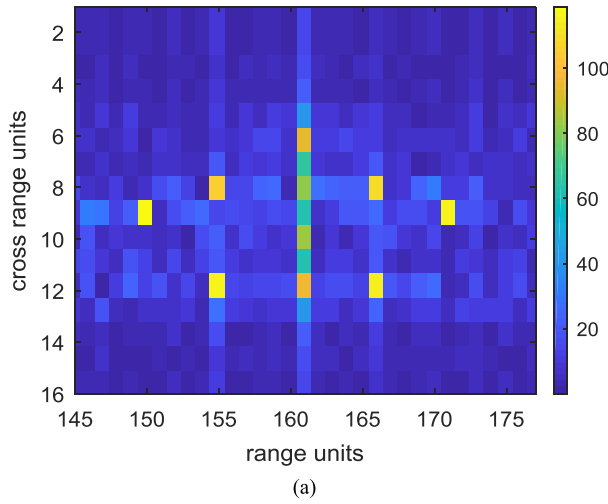


Fig. 15. Imaging results under different conditions using the MIMO radar system. (a) MIMO only. (b) MIMO + ISAR without time selection. (c) MIMO + ISAR with time selection.

appearing in the amplified images, as shown in Fig. 18. This is because the gaps in the cross-range direction mean that the time samples cannot be arranged uniformly, and thus, they cannot be equivalent to the spatial samples they are supposed to replace.

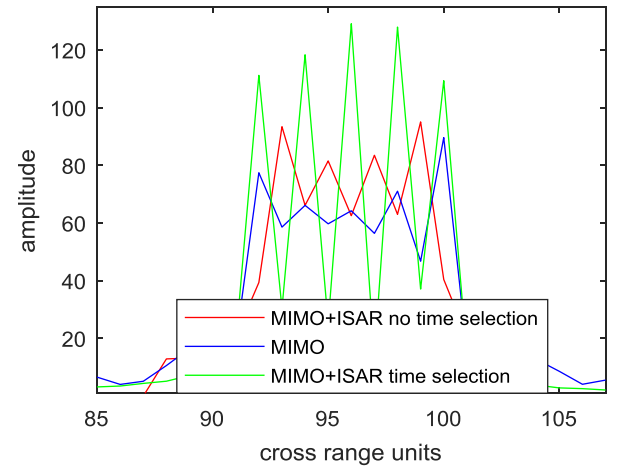


Fig. 16. Cross-range resolution comparison.

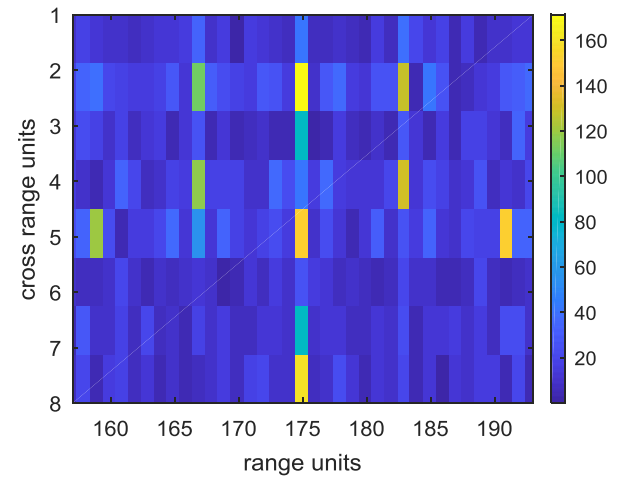


Fig. 17. Imaging result in the MIMO radar system.

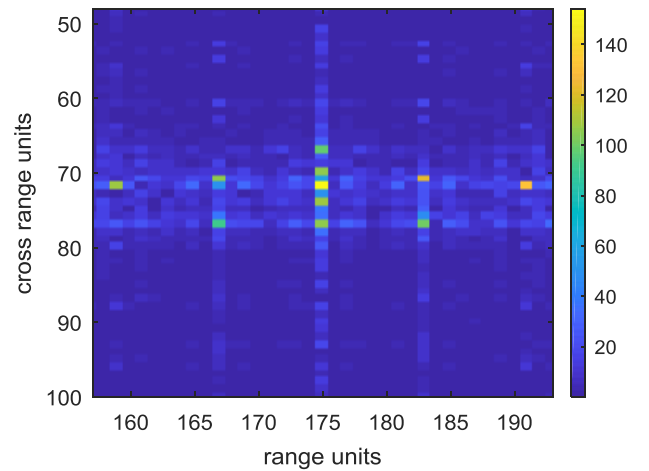


Fig. 18. Amplified image of MIMO + ISAR + Fourier transform.

Fig. 19 shows the imaging result by adopting the interpolation as suggested in [31]. Apparently, the false data introduced by the interpolation damages the imaging results in a way since the estimated data are not accurate when the structure of the echoes are complex.

Instead, if we adopt the CS technique to solve the problem, the imaging results will be much better. This is because



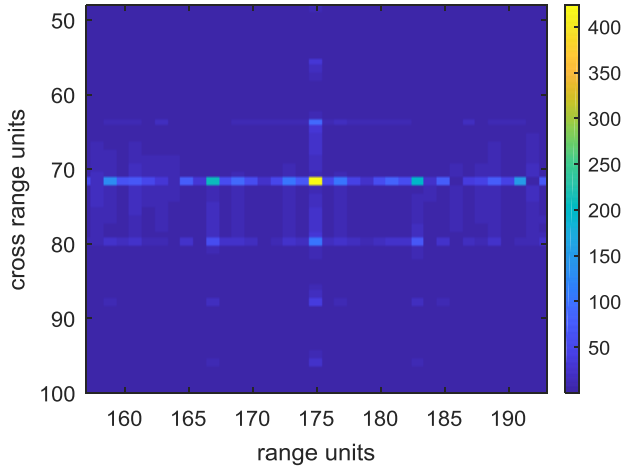


Fig. 19. Imaging results with interpolation.

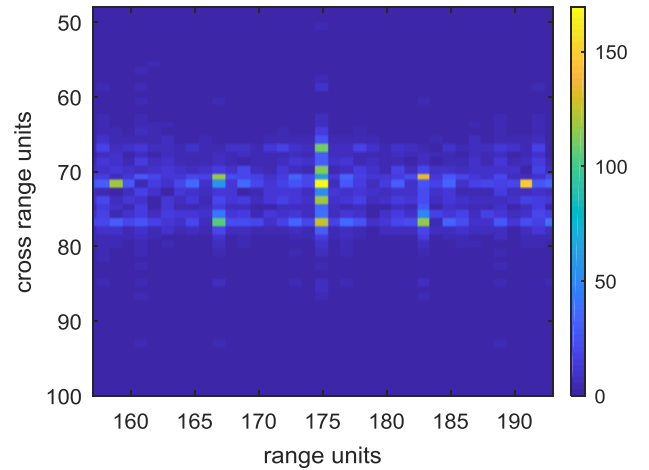


Fig. 21. Amplified image of MIMO + ISAR + SBL.

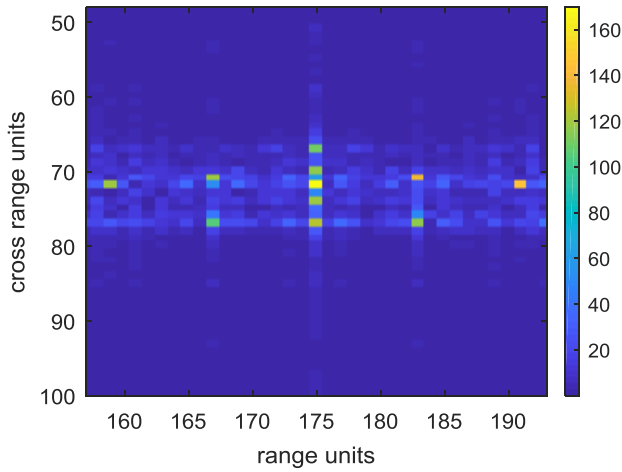


Fig. 20. Amplified image of MIMO + ISAR + SL0.

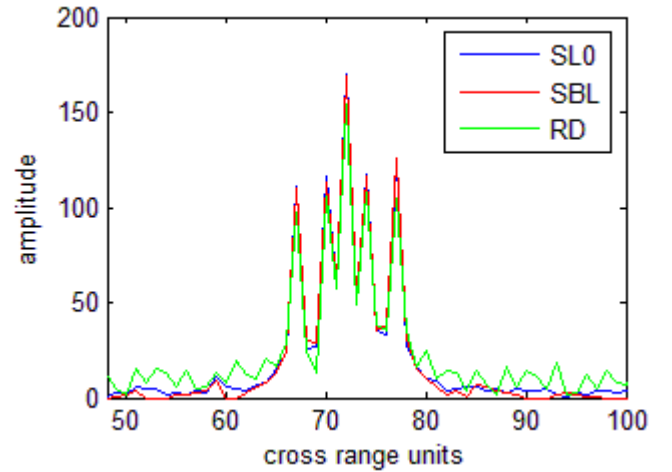


Fig. 22. Cross-range resolution comparison.

the gaps can just be regarded as missing data in continuous samples. In this experiment, we use the CS techniques based on SL0 and SBL to realize the imaging process. The reason for choosing these two kinds of CS methods is that both of the novel CS methods show better performance compared with other CS algorithms, which have been demonstrated explicitly in [20], [38], and [48]. Besides, since the CS algorithm especially for the 2-D signals which will be used in the following experiments is constructed on the basis of SL0 method, and cannot be replaced by other CS methods, therefore, the performance of the SL0 method has a direct relation with the performance of the CS method especially designed for the 2-D signals. As a result, some simple comparisons will be made between the SL0 method and the SBL method in order to substantiate the effectiveness of the SL0 method used in this paper is suitable enough both for the 1-D signals and the 2-D signals.

Figs. 20 and 21 show the imaging results by using the SL0 method and the SBL method, respectively.

Fig. 22 shows the resolution in the cross-range direction in the middle of the target by using three different methods, where the blue line, the red line, and the green line represent

the results obtained by adopting SL0, SBL, and Fourier transforms, respectively. It is easy to see that in Figs. 20 and 21, there are no false scatterers in the cross-range direction. Therefore, there will not be so many large amplitude side lobes in the imaging results using the two kinds of CS methods, as shown in Fig. 22.

The image entropies and the computation time of the three kinds of imaging methods are shown in Table III, where we only compare the computation time through using the algorithms in the CS technique since it is obvious that imaging through traditional Fourier transform will take less time. It is found that the imaging entropies based on SL0 and SBL methods are less than the entropy obtained by taking the Fourier transform directly. And the SL0 method enjoys shorter computation time.

In order to prove that the SL0 method is no less effective compared with other CS methods, such as the SBL method, in solving the imaging problem considered in this paper, the Monte Carlo experiments are conducted to show some specific performance of the SL0 method compared with the SBL method, and the results are shown in Figs. 23–25, where the blue line represents the results obtained by taking

TABLE III  
IMAGES ENTROPY AND THE COMPUTATIONAL TIME  
OF THE THREE METHODS

	MIMO+ISAR	SL0	SBL
Entropy	17.5533	16.8232	16.8310
Time(s)	/	2.8581	71.1921

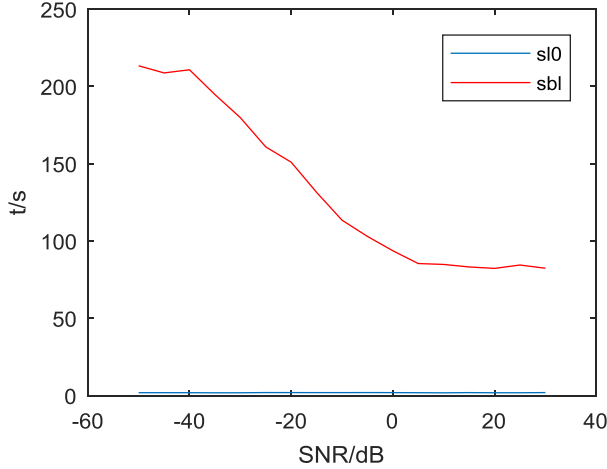


Fig. 23. Computational time comparison with the change of SNR.

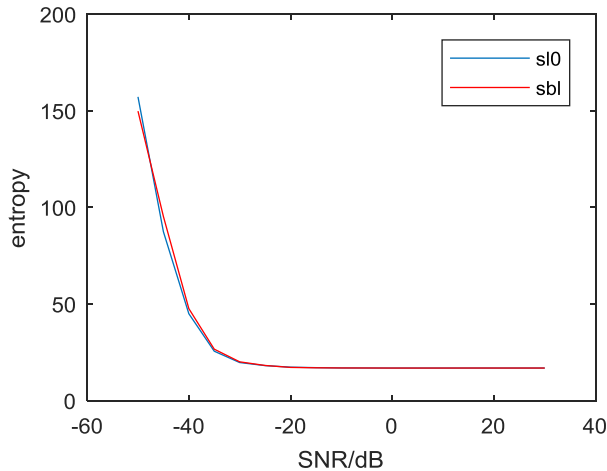


Fig. 24. Entropy comparison with the change of SNR.

SL0 method and the red line represents the results obtained by taking SBL method. Fig. 23 shows the changes of the computation time for two different methods as a function of SNR. It could be seen that the computation time of the SL0 method is shorter than that of the SBL method. Fig. 24 shows the changes of entropies for the two methods as a function of SNR. It could be seen that the two methods obtain similar imaging entropies with different SNRs.

In Figs. 23 and 24, the corresponding values of SNR varies from  $-50$  to  $30$  dB with an interval of  $5$  dB. Then, the performance of SL0 and SBL algorithms in the MIMO ISAR imaging can be reflected. Fig. 25 shows the changes of entropy for the two methods based on the changes in the imaging time on the condition that the gap always exists. We can find that the SL0 method and the SBL method share the similar

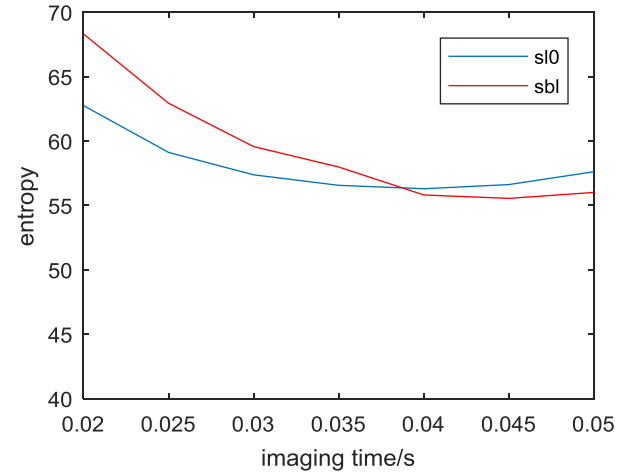


Fig. 25. Entropy comparison with the change of imaging time.

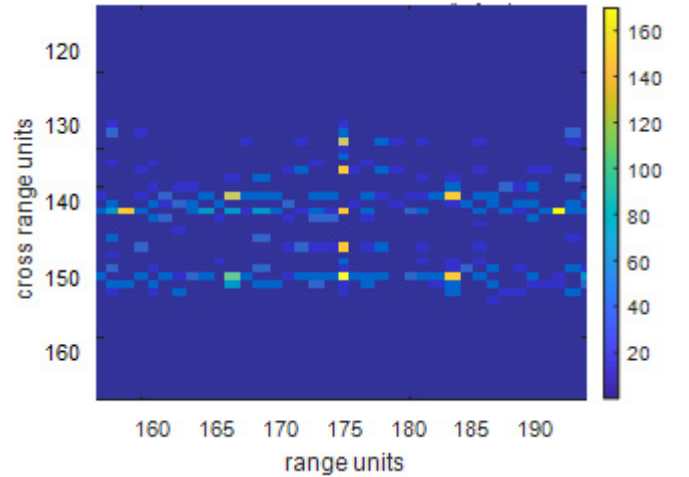


Fig. 26. Imaging result based on the SL0 method.

performance when the imaging time is increasing. All these results can prove that the SL0 method is not worse than other CS algorithms in solving the imaging problems in this paper.

What is more, since the CS technique has the ability for sparse reconstruction, the computational load can be reduced by taking this kind of approach. Here, using the example in the situation 2, we use the SL0 method and the SBL method to reconstruct the imaging results with twice the number of samples available and the corresponding results are shown in Figs. 26 and 27, respectively. It could be seen that the resolution of the image is still very good, and the imaging time and the number of the antenna elements has not increased.

### C. Experiment 3: Planar Array

In this experiment, the algorithms above will be extended to planar arrays in order to obtain 3-D information about the targets. In this experiment, we still use the target model and the system parameters in experiment 1. It is assumed that  $M_1 = M_2 = 4$ ,  $N_1 = N_2 = 8$ ,  $d_t = N_2 d_r = 120$  m,  $u_{t0} = -120$  m,  $v_{t0} = 120$  m,  $u_{r0} = -51.5$  m, and  $v_{r0} = 51.5$  m. The planar antenna array as shown in Fig. 28 can be obtained.

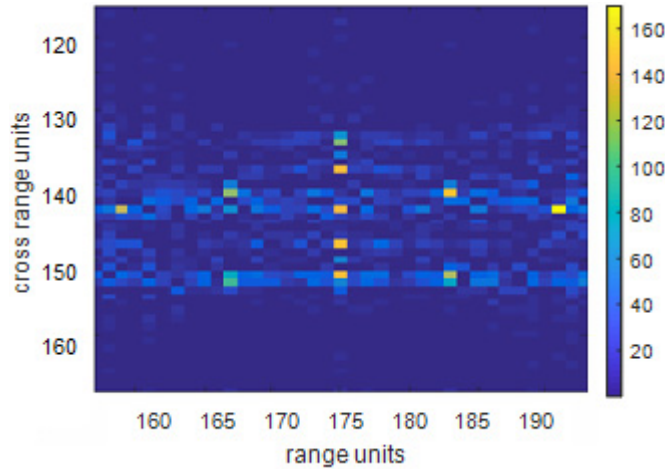


Fig. 27. Imaging result based on the SBL method.

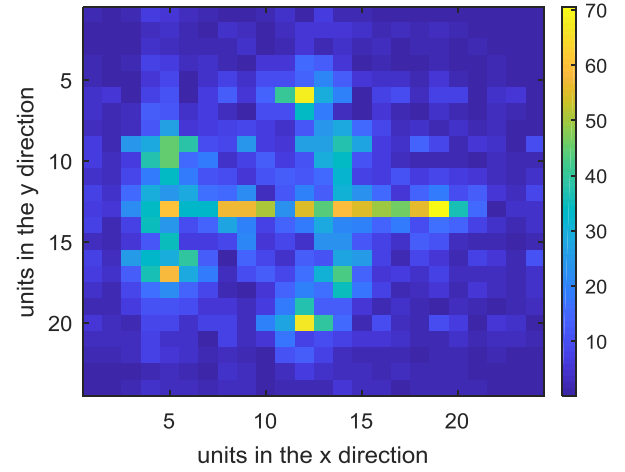


Fig. 29. Imaging result in the MIMO radar system.

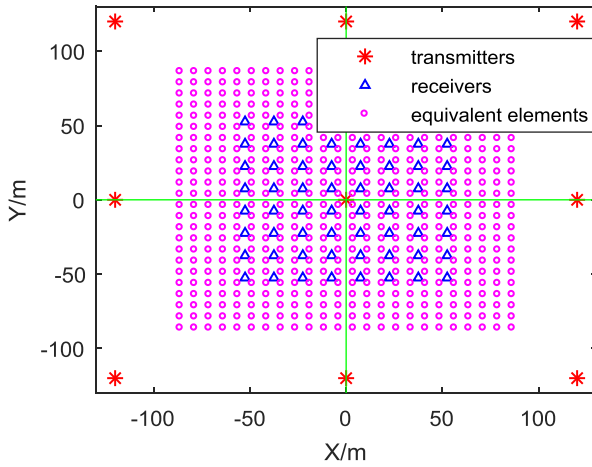
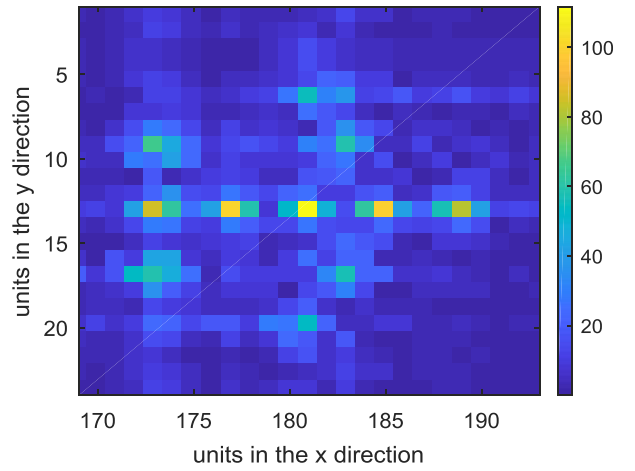


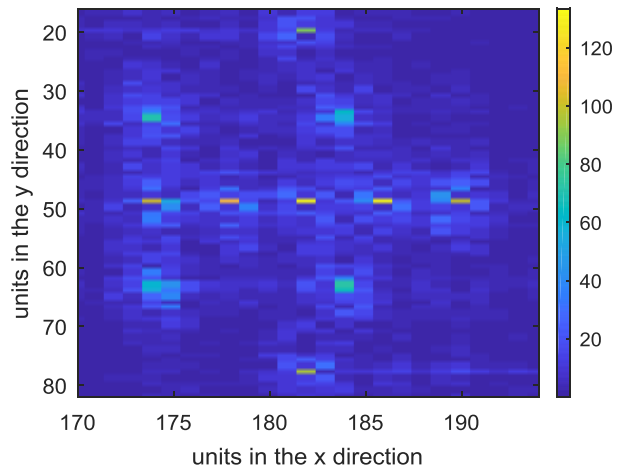
Fig. 28. Antenna array in experiment 3.

1) *Situation 1*: In this situation, the imaging time is set to be 0.1 s ( $P = 40$ ). The initial position of the target in the coordinate system ( $O, X, Y, Z$ ) is  $(0, 0, 10000)$  m.  $v = -300$  m/s,  $\alpha^* = 0$ , and  $\theta^* = \pi/4$ . Hence, the requirement of (21) has been met in the  $x$ - and  $y$ -directions. Here, the time samples are arranged along the  $x$ -direction. Fig. 29 shows the imaging result using the MIMO radar system. We find that since the numbers of the antenna elements in the two directions are limited, the scatterers are not separated very well. Fig. 30 shows the imaging result after bringing in the ISAR technique, and Fig. 30(a) shows the amplified image around the area where the target is located. It is shown that the resolution in the  $x$ -direction has been improved. On the basis of that, we use the 2D-SL0 algorithm and reconstruct the image with four times the number of sample points in the  $y$ -direction as before. Then, we can obtain Fig. 30(b). It could be seen that the image has better resolution without bringing in any estimated data or increasing the computation load.

2) *Situation 2*: In this situation, the imaging time is set to be 0.02 s ( $P = 8$ ). The initial position of the target in the coordinate system ( $O, X, Y, Z$ ) is  $(0, 0, 10000)$  m.  $v = -300$  m/s,  $\alpha^* = 0$ , and  $\theta^* = \pi/3$ . Hence, the requirement



(a)



(b)

Fig. 30. Imaging results before and after adopting the 2-D SL0 method. (a) Amplified image. (b) Imaging result based on the 2-D SL0 method.

of (21) has not been met in the both  $x$ - and  $y$ -directions, which means that there will be gaps between the signals received by different equivalent transceivers. Here, we still arrange the

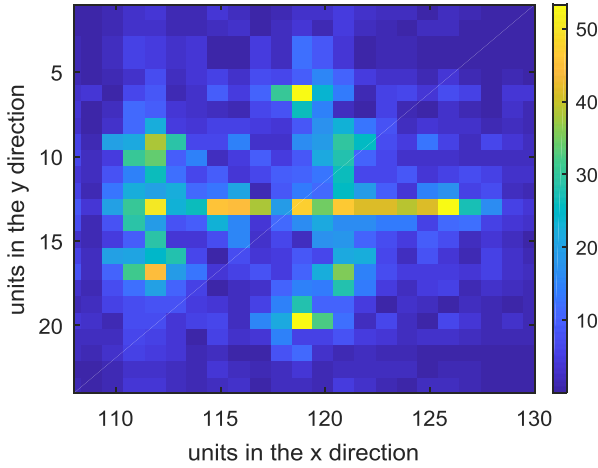


Fig. 31. Imaging results based on the Fourier transform.

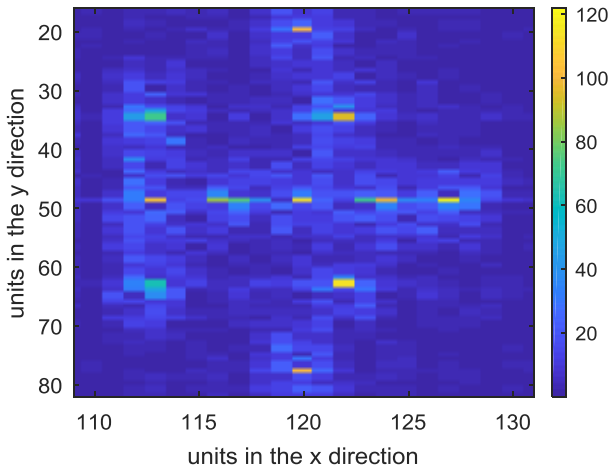


Fig. 32. Imaging results based on the SL0 method.

time samples in the  $x$ -direction. If we take Fourier transforms in the two directions directly, there will be many false scatterers in the image obtained, as shown in Fig. 31. According to the experience in experiment 2, we will not try to improve the resolution through interpolation since the estimated data may make the imaging results become worse, and compared with 1-D signals, it is more difficult to estimate the accurate data for 2-D signals to interpolate. Here, we choose to use the 2D-SL0 method to reconstruct the image with 4 times the number of samples in the  $y$ -direction as before. The final imaging result is shown in Fig. 32. It can be seen that there is no false target in the  $x$ -direction anymore. It could be found that the scatterers in the image have been separated successfully without bringing in any estimated data or increasing the computational load. As a result, the experiment can be used to prove that the algorithm mentioned in this paper is effective.

#### D. Experiment 4: 3-D Reconstruction

In this experiment, we use the results obtained in situation 1 of experiment 3 to reconstruct the 3-D coordinates of the target, and the results are shown in Fig. 33, where blue points represent the true positions of the scatterers and the red circles represent the positions of the reconstructed scatterers. From

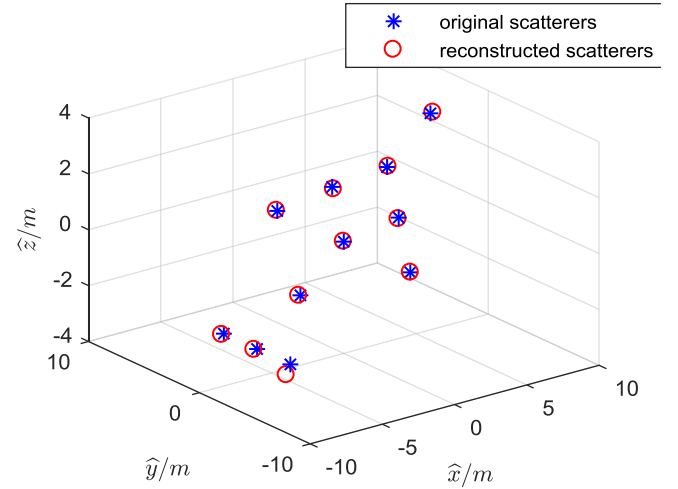


Fig. 33. 3-D coordinate reconstruction of the target.

Fig. 33, it is easy to see that most scatterers are reconstructed successfully. Even though one scatterer is not reconstructed accurately, it will not have the obvious effect on the final reconstructed results since most scatterers are reconstructed accurately, and the whole shape of the target has been formed correctly.

All the experiments results obtained above can be used to prove the effectiveness of the algorithm proposed in this paper.

*Remark 1:* Although the methods in this paper and the methods in [47] and [48] share some similar approximations, the parameter estimation process is quite different. Based on the characteristics of the radar configuration designed, the method in this paper takes advantage of the relationships between the adjacent transceivers to estimate the required parameters. The estimation process can be completed in the signal domain. Instead, the method in [47] and [48] use the information of the signals in the transformed domain to estimate the corresponding parameters, and no extra outside information except for the echoes, such as the location relationships between the transceivers in this method, is included, as a result, the estimation performance may be not that ideal when the imaging conditions are changed and the performance will not be very good when applied in this paper.

*Remark 2:* The purpose of designing experiment 2 is to compare the method in this paper with the methods mentioned in [31], and it has been explained that the reason why it is superior to the interpolation-based method is that the relations between the signals in the adjacent positions are very complex, the existing interpolation methods cannot predict the missing data correctly. Thus, it leads to the bad imaging results. We use the CS-based methods to realize the imaging process since the technique can be used to recover the signals almost correctly even when there is missing data. The involvement of point spread function is not necessary since it is not a typical way to evaluate the performance of the CS technique. As for the influence to the reconstruction brought by differences of the number and the coordinates of the scatterers, we have to say that the number and the coordinates of the scatterers will surely bring some influences to the final imaging results. Finally,



for the velocity estimation errors, the performance will not degrade in the presence of gapped data, since we can only use the adjacent signals to estimate the velocity. If there are errors in the velocity estimation, then the time delay calculated based on the estimated velocity in Section III will not be correct, which means that there may be gaps or overlapping parts between the adjacent combined signals according to (54), then the whole combined signals will be destroyed. The time samples will not be equivalent to the space samples anymore.

## VII. CONCLUSION

In this paper, we propose a novel 3-D imaging method by introducing the ISAR technique to the MIMO radar system. Referring to [30], the special algorithm used for combining the signals received by different transceivers in the radar configuration proposed in this paper is adopted. The simulation results show that the adopted algorithm can realize better imaging resolution compared with the algorithm in [31]. Besides, for the situation where there are gaps in the global observation angles, the CS technique is used to replace the traditional interpolation process utilized in similar situations. The simulation results show that by taking the CS technique, extra false targets can be removed from the imaging results obtained by utilizing the incomplete data, and no estimated data is introduced as happens in situations where the interpolation process is adopted. Thus, the imaging results can reflect the true information about the targets. Furthermore, in the situation where the planar antenna array is conducted, the adoption of 2D-SLO method, which is especially designed for the 2-D signals, helps to reconstruct the imaging results with fewer antenna elements and less computation load, which enables the 3-D imaging technique that combines the ISAR technique and the MIMO radar system to be better realized in real applications. Finally, the algorithms for the range alignment and the velocity estimation which are designed specifically after taking the characteristics of the radar configuration adopted in this paper into consideration are described explicitly. The final successful 3-D reconstruction of the imaging targets substantiates that the 3-D imaging method that combines the ISAR technique and the MIMO radar system presented in this paper is effective enough to reflect the true information of the imaging targets.

## REFERENCES

- [1] F. Berizzi, E. D. Mese, M. Diani, and M. Martorella, "High-resolution ISAR imaging of maneuvering targets by means of the range instantaneous Doppler technique: Modeling and performance analysis," *IEEE Trans. Image Process.*, vol. 10, no. 12, pp. 1880–1890, Dec. 2001.
- [2] Z. Bao, C. Sun, and M. Xing, "Time-frequency approaches to ISAR imaging of maneuvering targets and their limitations," *IEEE Trans. Aerosp. Electron. Syst.*, vol. 37, no. 3, pp. 1091–1099, Jul. 2001.
- [3] T. Thayaparan, G. Lampropoulos, S. K. Wong, and E. Riseborough, "Application of adaptive joint time-frequency algorithm for focusing distorted ISAR images from simulated and measured radar data," *IEE Proc.-Radar, Sonar Navigat.*, vol. 150, no. 4, pp. 213–220, Aug. 2003.
- [4] T. Thayaparan, L. J. Stankovic, C. Wernik, and M. Dakovic, "Real-time motion compensation, image formation and image enhancement of moving targets in ISAR and SAR using S-method based approach," *IET Signal Process.*, vol. 2, no. 3, pp. 247–264, Sep. 2008.
- [5] Y. Wang and Y. Lin, "ISAR imaging of non-uniformly rotating target via range-instantaneous-Doppler-derivatives algorithm," *IEEE J. Sel. Topics Appl. Earth Observ. Remote Sens.*, vol. 7, no. 1, pp. 167–176, Jan. 2014.
- [6] Y. Wang, "Inverse synthetic aperture radar imaging of manoeuvring target based on range-instantaneous-Doppler and range-instantaneous-chirp-rate algorithms," *IET Radar, Sonar Navigat.*, vol. 6, no. 9, pp. 921–928, Dec. 2012.
- [7] X.-G. Xia, G. Wang, and V. C. Chen, "Quantitative SNR analysis for ISAR imaging using joint time-frequency analysis-short time Fourier transform," *IEEE Trans. Aerosp. Electron. Syst.*, vol. 38, no. 2, pp. 649–659, Apr. 2002.
- [8] Y. Wang, B. Zhao, and Y. Jiang, "Inverse synthetic aperture radar imaging of targets with complex motion based on cubic Chirplet decomposition," *IET Signal Process.*, vol. 9, no. 5, pp. 419–429, Jul. 2015.
- [9] X. Bai, R. Tao, Z. Wang, and Y. Wang, "ISAR imaging of a ship target based on parameter estimation of multicomponent quadratic frequency-modulated signals," *IEEE Trans. Geosci. Remote Sens.*, vol. 52, no. 2, pp. 1418–1429, Feb. 2013.
- [10] S. K. Wong, G. Duff, and E. Riseborough, "Distortion in the inverse synthetic aperture radar (ISAR) images of a target with time-varying perturbed motion," *IEE Proc.-Radar Sonar Navigat.*, vol. 150, no. 4, pp. 221–227, Aug. 2003.
- [11] W. Qiu, M. Martorella, J. Zhou, H. Zhao, and Q. Fu, "Three-dimensional inverse synthetic aperture radar imaging based on compressive sensing," *IEE Proc.-Radar, Sonar Navigat.*, vol. 9, no. 4, pp. 411–420, Apr. 2014.
- [12] M. Martorella, D. Stagliano, F. Salvetti, and N. Battisti, "3D interferometric ISAR imaging of noncooperative targets," *IEEE Trans. Aerosp. Electron. Syst.*, vol. 50, no. 4, pp. 3102–3114, Oct. 2014.
- [13] L. Liu, F. Zhou, X.-R. Bai, M.-L. Tao, and Z.-J. Zhang, "Joint cross-range scaling and 3D geometry reconstruction of ISAR targets based on factorization method," *IEEE Trans. Image Process.*, vol. 25, no. 4, pp. 1740–1750, Apr. 2016.
- [14] Q. Zhang and T. S. Yeo, "Three-dimensional SAR imaging of a ground moving target using the InISAR technique," *IEEE Trans. Geosci. Remote Sens.*, vol. 42, no. 9, pp. 1818–1828, Sep. 2004.
- [15] C. Ma, T. Yeo, and C. Tan, "Three-dimensional imaging of targets using colocated MIMO radar," *IEEE Trans. Geosci. Remote Sens.*, vol. 49, no. 8, pp. 3009–3021, Aug. 2011.
- [16] G. Q. Duan, D. W. Wang, X. Y. Ma, and Y. Su, "Three-dimensional imaging via wideband MIMO radar system," *IEEE Geosci. Remote Sens. Lett.*, vol. 7, no. 3, pp. 445–449, Jul. 2010.
- [17] C. Ma, T. S. Yeo, Q. Zhang, H. S. Tan, and J. Wang, "Three-dimensional ISAR imaging based on antenna array," *IEEE Trans. Geosci. Remote Sens.*, vol. 46, no. 2, pp. 504–515, Feb. 2008.
- [18] R. Bhalla and H. Ling, "Three-dimensional scattering center extraction using the shooting and bouncing ray technique," *IEEE Trans. Antennas Propag.*, vol. 44, no. 11, pp. 1445–1453, Nov. 1996.
- [19] J. T. Mayhan, M. L. Burrows, K. M. Cuomo, and J. E. Piou, "High resolution 3D 'snapshot' ISAR imaging and feature extraction," *IEEE Trans. Aerosp. Electron. Syst.*, vol. 37, no. 2, pp. 630–642, Apr. 2001.
- [20] C. Ma, T. S. Yeo, Y. Zhao, and J. Feng, "MIMO radar 3D imaging based on combined amplitude and total variation cost function with sequential order one negative exponential form," *IEEE Trans. Image Process.*, vol. 23, no. 5, pp. 2168–2183, May 2014.
- [21] X. Xu and R. M. Narayanan, "Three-dimensional interferometric ISAR imaging for target scattering diagnosis and modeling," *IEEE Trans. Image Process.*, vol. 10, no. 7, pp. 1094–1102, Jul. 2001.
- [22] C. Ma, T. S. Yeo, C. S. Tan, J.-Y. Li, and Y. Shang, "Three-dimensional imaging using colocated MIMO radar and ISAR technique," *IEEE Trans. Geosci. Remote Sens.*, vol. 50, no. 8, pp. 3189–3201, Aug. 2012.
- [23] X. Cao, F. Su, H. Sun, and G. Xu, "Three-dimensional In-ISAR imaging via the emulated bistatic radar," in *Proc. IEEE Conf. Ind. Electron. Appl.*, May 2007, pp. 2826–2830.
- [24] G. Wang, X.-G. Xia, and V. C. Chen, "Three-dimensional ISAR imaging of maneuvering targets using three receivers," *IEEE Trans. Image Process.*, vol. 10, no. 3, pp. 436–447, Mar. 2001.
- [25] N. Battisti and M. Martorella, "Interferometric phase and target motion estimation for accurate 3D reflectivity reconstruction in ISAR systems," in *Proc. IEEE Radar Conf.*, May 2010, pp. 108–112.
- [26] A. Bellettini and M. A. Pinto, "Theoretical accuracy of synthetic aperture sonar microneavigation using a displaced phase-center antenna," *IEEE J. Ocean. Eng.*, vol. 27, no. 4, pp. 780–789, Oct. 2002.
- [27] J. Li and P. Stoica, *MIMO Radar Signal Processing*. Hoboken, NJ, USA: Wiley, 2009.
- [28] J. Li and P. Stoica, "MIMO radar with colocated antennas," *IEEE Signal Process. Mag.*, vol. 24, no. 5, pp. 106–114, Sep. 2007.
- [29] A. M. Haimovich, R. S. Blum, and L. J. Cimini, "MIMO radar with widely separated antennas," *IEEE Signal Process. Mag.*, vol. 25, no. 1, pp. 116–129, Jan. 2008.

- [30] D. Pastina, M. Bucciarelli, and P. Lombardo, "Multistatic and MIMO distributed ISAR for enhanced cross-range resolution of rotating targets," *IEEE Trans. Geosci. Remote Sens.*, vol. 48, no. 8, pp. 3300–3317, Aug. 2010.
- [31] Y. Zhu, Y. Su, and W. Yu, "An ISAR imaging method based on MIMO technique," *IEEE Trans. Geosci. Remote Sens.*, vol. 48, no. 8, pp. 3290–3299, Aug. 2010.
- [32] Y. Zhu and Y. Su, "A type of  $M^2$ -transmitter  $N^2$ -receiver MIMO radar array and 3D imaging theory," *Sci. China Inf. Sci.*, vol. 54, no. 10, pp. 2147–2157, Oct. 2011.
- [33] L. Zhang *et al.*, "Resolution enhancement for inversed synthetic aperture radar imaging under low SNR via improved compressive sensing," *IEEE Trans. Geosci. Remote Sens.*, vol. 48, no. 10, pp. 3824–3838, Oct. 2010.
- [34] A. S. Khwaja and X.-P. Zhang, "Compressed sensing ISAR reconstruction in the presence of rotational acceleration," *IEEE J. Sel. Topics Appl. Earth Observ. Remote Sens.*, vol. 7, no. 7, pp. 2957–2970, Jul. 2014.
- [35] W. Rao, G. Li, X. Wang, and X.-G. Xia, "Adaptive sparse recovery by parametric weighted  $L_1$  minimization for ISAR imaging of uniformly rotating targets," *IEEE J. Sel. Topics Appl. Earth Observ. Remote Sens.*, vol. 6, no. 2, pp. 942–952, Apr. 2013.
- [36] G. Li, H. Zhang, X. Wang, and X.-G. Xia, "ISAR 2-D imaging of uniformly rotating targets via matching pursuit," *IEEE Trans. Aerosp. Electron. Syst.*, vol. 48, no. 2, pp. 1838–1846, Apr. 2012.
- [37] G. Li and P. K. Varshney, "Micro-Doppler parameter estimation via parametric sparse representation and pruned orthogonal matching pursuit," *IEEE J. Sel. Topics Appl. Earth Observ. Remote Sens.*, vol. 7, no. 12, pp. 4937–4948, Dec. 2014.
- [38] D.-W. Wang, X.-Y. Ma, A.-L. Chen, and Y. Su, "High-resolution imaging using a wideband MIMO radar system with two distributed arrays," *IEEE Trans. Image Process.*, vol. 19, no. 5, pp. 1280–1289, May 2010.
- [39] K. B. Petersen and M. S. Pedersen. (2008). *The Matrix Cookbook*. [Online]. Available: <http://matrixcookbook.com>
- [40] A. Ghaffari, M. Babaie-Zadeh, and C. Jutten, "Sparse decomposition of two dimensional signals," in *Proc. IEEE Int. Conf. Acoust., Speech Signal Process.*, Apr. 2009, pp. 3157–3160.
- [41] G. Mohimani, M. Babaie-Zadeh, and C. Jutten, "A fast approach for overcomplete sparse decomposition based on smoothed  $\ell^0$  norm," *IEEE Trans. Signal Process.*, vol. 57, no. 1, pp. 289–301, Jan. 2009.
- [42] N. Ma and J. T. Goh, "Efficient method to determine diagonal loading value," in *Proc. IEEE Int. Conf. Acoust., Speech Signal Process.*, vol. 5, Apr. 2003, pp. 341–344.
- [43] C.-C. Chen and H. C. Andrews, "Target-motion-induced radar imaging," *IEEE Trans. Aerosp. Electron. Syst.*, vol. AES-16, no. 1, pp. 2–14, Jan. 1980.
- [44] D. Zhu, L. Wang, Q. Tao, and Z. Zhu, "ISAR range alignment by minimizing the entropy of the average range profile," in *Proc. IEEE Conf. Radar*, Apr. 2006, pp. 813–818.
- [45] Q. Zhang, T. S. Yeo, G. Du, and S. H. Zhang, "Estimation of three-dimensional motion parameters in interferometric ISAR imaging," *IEEE Trans. Geosci. Remote Sens.*, vol. 42, no. 2, pp. 292–300, Feb. 2004.
- [46] M. Martorella, "Novel approach for ISAR image cross-range scaling," *IEEE Trans. Aerosp. Electron. Syst.*, vol. 44, no. 1, pp. 281–294, Jan. 2008.
- [47] D. Pastina, "Rotation motion estimation for high resolution ISAR and hybrid SAR/ISAR target imaging," in *Proc. IEEE Radar Conf.*, May 2008, pp. 1–6.
- [48] J. Wang and D. Kasilingam, "Global range alignment for ISAR," *IEEE Trans. Aerosp. Electron. Syst.*, vol. 39, no. 1, pp. 351–357, Jan. 2003.



**Yong Wang** (SM'16) was born in Fuyu, Jilin, China, in 1979. He received the B.S. and M.S. degrees in electronic engineering and the Ph.D. degree in information and communication engineering from the Harbin Institute of Technology (HIT), Harbin, China, in 2002, 2004, and 2008, respectively.

He is currently a Professor with the Institute of Electronic Engineering Technology, HIT. He has authored over 60 papers and most of them appeared in the journals of the IEEE TRANSACTIONS ON GEOSCIENCE AND REMOTE SENSING, the *IET Signal Processing*, and the *Signal Processing*. His research interests include the time–frequency analysis of nonstationary signal, radar signal processing, and their application in synthetic aperture radar imaging.

Dr. Wang was as recipient of the Program for New Century Excellent Talents in University of Ministry of Education of China in 2012 and the Excellent Doctor's Degree nomination Award in China in 2010.



**Xuelu Li** was born in Hohhot, China, in 1991. She received the B.S. and M.S. degrees in electronic engineering from the Harbin Institute of Technology, Harbin, China, in 2014 and 2016, respectively.

Her research interests include the field of interferometric inverse synthetic aperture radar imaging, time–frequency signal analysis, and superresolution imaging based on compressive sensing.